NASA Technical Memorandum 2002–206892, Volume 20

SeaWiFS Postlaunch Technical Report Series

Stanford B. Hooker, Editor
NASA Goddard Space Flight Center
Greenbelt, Maryland

Elaine R. Firestone, Senior Scientific Technical Editor
Science Applications International Corporation
Beltsville, Maryland

Volume 20, Coastal Atmosphere and Sea Time Series (CoASTS), Part 2: Data Analysis

Jean-François Berthon
Giuseppe Zibordi
John P. Doyle
Stefania Grossi
Dirk van der Linde
Cristina Targa
JRC Space Applications Institute
Ispra, Italy

Abstract

In this document, the first three years of a time series of bio-optical marine and atmospheric measurements are presented and analyzed. These measurements were performed from an oceanographic tower in the northern Adriatic Sea within the framework of the Coastal Atmosphere and Sea Time Series (CoASTS) project, an ocean color calibration and validation activity. The data set collected includes spectral measurements of the in-water apparent (diffuse attenuation coefficient, reflectance, Q-factor, etc.) and inherent (absorption and scattering coefficients) optical properties, as well as the concentrations of the main optical components (pigment and suspended matter concentrations). Clear seasonal patterns are exhibited by the marine quantities on which an appreciable short-term variability (on the order of a half day to one day) is superimposed. This short-term variability is well correlated with the changes in salinity at the surface resulting from the southward transport of freshwater coming from the northern rivers. Concentrations of chlorophyll *a* and total suspended matter span more than two orders of magnitude. The bio-optical characteristics of the measurement site pertain to both Case-1 (about 64%) and Case-2 (about 36%) waters, based on a relationship between the beam attenuation coefficient at 660 nm and the chlorophyll *a* concentration. Empirical algorithms relating in-water remote sensing reflectance ratios and optical components or properties of interest (chlorophyll *a*, total suspended matter, and the diffuse attenuation coefficient) are presented.

1. INTRODUCTION

The use of remotely-sensed ocean color data has increased considerably over the last years, since several new sensors were put in orbit more than 10 years after the Coastal Zone Color Scanner (CZCS) ceased its activity. These sensors, specifically, the Sea-viewing Wide Field-of-view Sensor (SeaWiFS), the Ocean Color and Temperature Scanner (OCTS), the Marine Optical Spectroradiometer (MOS), the Moderate Resolution Imaging Spectroradiometer (MODIS), and the Medium Resolution Imaging Spectrometer (MERIS), present advanced characteristics compared to CZCS, in the addition of a certain number of channels, and an increased signal-to-noise ratio and dynamic range (IOCCG 1998). These increased capacities are intended, in particular, to improve the retrieval of chlorophyll *a* concentration in the open ocean (Hooker et al. 1992 and O'Reilly et al. 1998), as well as eventually allowing the retrieval of additional marine quantities such as total suspended matter or colored dissolved organic matter (Carder et al. 1999).

For the open ocean, the possibility of retrieving chlorophyll *a* and additional water components from remotely-sensed data is presumably simplified, because in most cases, they all co-vary (but see Carder et al. 1991). In coastal waters (where most of the so-called optical "Case-2" waters can be found), however, this retrieval is less successful. In effect, because of the diversity of the sources (rivers, atmospheric input, bottom resuspension, etc.) the simplifying assumption of co-variation may not be verified. Consequently, by contributing—often antagonistically—to the total marine signal, the occurrence of these different components makes their separation much more difficult on an optical basis.

As a consequence of the number of sensors now operational, there is an increasing demand for *in situ* bio-optical data (water and atmosphere) in order to address two main topics:

1) The development of models and algorithms allowing the retrieval of marine and atmospheric quantities from the signal at the top of the atmosphere; and
2) The vicarious calibration of the sensors, and the validation of their different products.

Programs including time-series of measurements on specific sites such as the Marine Optical Buoy (MOBY, Clark et al. 1997), the Yamato Bank Optical Mooring (YBOM, Kishino et al. 1997), and the Plymouth Marine Bio-Optical Data Buoy (PlyMBODy, Pinkerton and Aiken 1999), or repetitive ship cruises such as the Atlantic Meridional Transect (AMT) program (Aiken et al. 2000) were developed considerably in the past years. Basing the investigation of the environment on a long time or space scale, one of their objectives was, in particular, to encompass a wide range of optical properties and concentration of optically significant components.

In this context, a program of extensive *in situ* measurements called the Coastal Atmosphere and Sea Time Series (CoASTS), was set up (Zibordi et al. 2002). Within this program, a series of marine and atmospheric measurements are performed from an oceanographic tower located in the northern Adriatic Sea, off the Venice Lagoon. As of this writing, the project has provided more than six years of data (with a frequency of 1–2 campaigns per month) including water apparent and inherent optical properties and the corresponding optically significant components, as well as atmospheric measurements, which allows for the estimation of aerosol properties. The resulting data set was

partially presented (Berthon et al. 1998, 2000, 2001; and Zibordi and Berthon 2001) and used for radiative transfer computations (Zibordi et al. 1999), and calibration and validation activities (Sturm and Zibordi 2002).

This report is aimed at presenting the CoASTS data from October 1995 to December 1998, in particular by giving emphasis to a number of items:

1) The variability at different time scales of some relevant quantities (the main optical components and their inherent optical properties, the apparent optical properties of the water column, etc.);
2) Inter-relationships between quantities to be used in the development of bio-optical models; and
3) Local algorithms relating the concentration of total chlorophyll *a* (C_a) and the concentration of total suspended matter (C_{TSM}).

2. DATA AND METHODS

Within the framework of the CoASTS project, the Joint Research Centre with the contribution of the Italian National Research Council, has sponsored measurements that are performed from the *Acqua Alta* Oceanographic Tower (AAOT), located in the northern Adriatic Sea, off the Venice Lagoon (45.310°N,12.510°E). Measurement campaigns lasting a few days, take place every 2–4 weeks according to the season and can include from 3–10 sets of comprehensive measurements (or *stations*) each.

The measurements conducted during the periodic field campaigns include in-water profiles of the apparent and inherent optical properties of the light field, discrete water samples at different depths (near-surface, 8 m, and 14 m; the bottom is at 17 m) for biogeochemical analysis, temperature and conductivity profiles, sky radiance, sun irradiance, and meteorological data. The CoASTS data set presented here includes 269 stations (October 1995–December 1998). A detailed description of the instruments, measurement methodologies, and uncertainties is given in Zibordi et al. (2002).

3. DATA ANALYSIS

In this section, the time series of the marine and atmospheric measurements are presented and discussed.

3.1 Environmental Characteristics

The surface circulation in the northern Adriatic Sea is dominated by the North Adriatic (NAd) current which flows southward along the Italian northeastern coast, with a maximal southward extension during the boreal spring. In the boreal autumn, the surface circulation is primarily determined by the North Adriatic cyclonic gyre, which develops at the latitude of the Po River outflow (Artegiani et al. 1997b). Hydrological features at the tower site are primarily influenced by the northern river discharges (conveyed by the NAd current), as well as by wind and rain variability, and consequently are susceptible to very short time-scale variations, which are superimposed on the main seasonal evolution.

3.1.1 Meteorological Conditions

In Table 1, data are presented of the average seasonal values of some meteorological variables (air temperature, relative humidity, atmospheric pressure, wind speed, and direction) instantaneously measured at the platform site at the time of sampling. The use of the calendar months for partitioning the seasons is in agreement with Zavatarelli et al. (1998) and it maintains coherence with the usual seasonal cycle of river discharge. A direct comparison can, therefore, be made with the climatology of biogeochemical variables presented in the latter work.

Air temperature, T_a, exhibits a total variation of 25°C with a minimum around 3°C in January 1998 (an exceptional unique value of 0.3°C was observed in January 1996) and a maximum around 28°C in August 1998. The observed seasonal cycle is in good agreement with the mean climatology presented by Artegiani et al. (1997a). Relative humidity (RH), although highly variable at short time scale, presents average maximum values in spring† (April–May–June) of 78.8%, and minimum values in winter (January–February–March) of 61.7%.

Wind speed (W_s) and wind direction (W_d) measured at the time of sampling are highly variable and no clear cycle is discernible. The strongest and lightest winds, however, are generally observed during the winter and autumn (October–November–December), respectively. Northeasterly (0–90°) and southeasterly (90–180°) winds generally dominate, but abrupt changes in wind direction have frequently been observed during a field campaign. No particular correlation has been observed between wind speed and direction. Because measurements are not performed when weather conditions are too severe, which is usually associated with low atmospheric pressure (P_a), the time series of meteorological data may not be fully representative of the site conditions during the year.

3.1.2 Near-Surface Temperature and Salinity

The near-surface values of seawater salinity S_w and temperature T_w presented here correspond to the average value within the near-surface layer (for a depth ranging from 1–2 m) and computed from conductivity, temperature, and depth (CTD), vertical profiles performed during sampling stations. Density excess, γ, was computed according to the UNESCO (1981) formulation without including pressure effects. Average global and seasonal values for these quantities are presented in Table 1.

† References throughout this document to seasons of the year are to the seasons of the Northern Hemisphere and are defined on first usage.

Table 1. Marine and atmospheric parameters for the entire (global) data set and a seasonal partitioning of the data: January–February–March (JFM), April–May–June (AMJ), July–August–September (JAS), and October–November–December (OND). For each variable (X), X_n is the number of samples, $\bar{X}$ is the average, X_σ is the standard deviation, X^- is the minimum value, and X^+ is the maximum value.

Period	*Statistic*	T_a [°C]	RH [%]	P_a [hPa]	W_s [m s^{-1}]	W_d [°]	T_w [°C]	S_w [PSU]	γ [kg m^{-3}]
Global	X_n	259	265	268	247	238	269	269	269
	$\bar{X}$	15.84	71.1	1020.16	3.31	144.0	16.907	34.978	25.373
	X_σ	6.82	17.0	6.87	1.90	107.5	5.913	1.774	2.326
	X^-	0.3	24	1000.5	0.0	0	7.31	30.54	19.67
	X^+	28.2	100	1036.7	9.1	360	27.36	38.05	29.60
JFM	X_n	56	63	63	63	62	64	64	64
	$\bar{X}$	7.82	61.7	1024.31	3.74	137.7	9.740	36.121	27.870
	X_σ	2.89	19.4	8.19	1.89	121.5	0.914	1.836	1.447
	X^-	0.3	24	1002.2	0.0	0	7.31	31.93	24.43
	X^+	13.9	99	1036.7	8.6	360	11.66	38.05	29.60
AMJ	X_n	68	65	68	63	61	68	68	68
	$\bar{X}$	17.39	78.8	1018.76	3.26	144.1	17.816	34.375	24.759
	X_σ	4.16	11.6	6.87	2.02	84.3	4.402	1.475	1.756
	X^-	8.4	57	1000.5	0.0	5	11.18	30.89	20.33
	X^+	26.0	99	1035.4	8.4	332	24.84	37.28	28.52
JAS	X_n	61	63	63	47	43	63	63	63
	$\bar{X}$	23.63	74.9	1018.19	3.55	119.3	24.283	34.258	22.988
	X_σ	2.38	17.2	4.21	2.14	86.9	1.731	1.574	1.545
	X^-	17.5	24	1004.7	0.0	6	20.28	30.54	19.67
	X^+	28.2	99	1025.0	9.1	341	27.36	36.89	25.44
OND	X_n	74	74	74	74	72	74	74	74
	$\bar{X}$	14.06	68.9	1019.59	2.82	164.1	15.991	35.156	25.809
	X_σ	5.67	14.6	6.08	1.51	120.8	3.702	1.607	1.513
	X^-	3.1	37	1008.0	0.0	0	8.20	30.67	23.12
	X^+	23.0	100	1031.2	8.0	360	21.01	37.60	28.66

The seasonal cycle for near-surface temperature (Fig. 1) closely follows the air temperature, with the minimum (about 6–8°C) in January–February and the maximum (around 26–28°C) in July–August. This cycle is in good agreement with the seasonal climatology provided by Artegiani et al. (1997b). Minor *intra-campaign* changes (around 1°C) are usually observed except for campaigns 21 (10–7.5°C), 37 (11–9°C) and 44 (22.5–24.5°C) for which variations larger than 2°C were recorded. These short-term variations are frequently observed in conjunction with the presence of less saline water transported to the site. The latter is usually seen as a thin (about 2 m thick), generally cooler, surface layer. A variation of about 2°C (from 21–19°C), due to the mixing of the water column induced by high winds, can also be observed for campaign 11. In this last case, near-surface salinity increases from 33.5–35 PSU after mixing with more saline subsurface waters.

High salinity at the surface (Fig. 1), with a maximum around 38 PSU, is systematically associated with the winter months, whereas minimum values are irregularly distributed within the year. Very low values, from 30–31 PSU, were observed in October 1996 (campaign 20) and, to a lesser extent, in July 1997 (campaign 31) and June 1998 (campaign 44). Note that anomalous high air temperature (and low atmospheric pressure) were also observed during campaign 20.

The 1996 campaign year departed from the mean climatology proposed by Artegiani et al. (1997b), by globally showing higher values (differences up to 4–5 PSU), whereas years 1997 and 1998 more closely followed it. Rapid changes, on the order of 2–4 PSU in the near-surface salinity, were frequently observed.† These changes are primarily due to variations in the extension toward the east of the southward flowing coastal current carrying low salinity waters from the northern rivers.

3.1.3 Vertical Distribution of T_w and S_w

The average seasonal vertical profiles of temperature and salinity are presented in Fig. 2. In winter (Figs. 2a and b), cold waters extend from the surface down to the

† These changes were seen during campaigns 8, 11, 13, 21, 22, 30, 31, 36, 37, 39, 41, 43, 44, and 50.

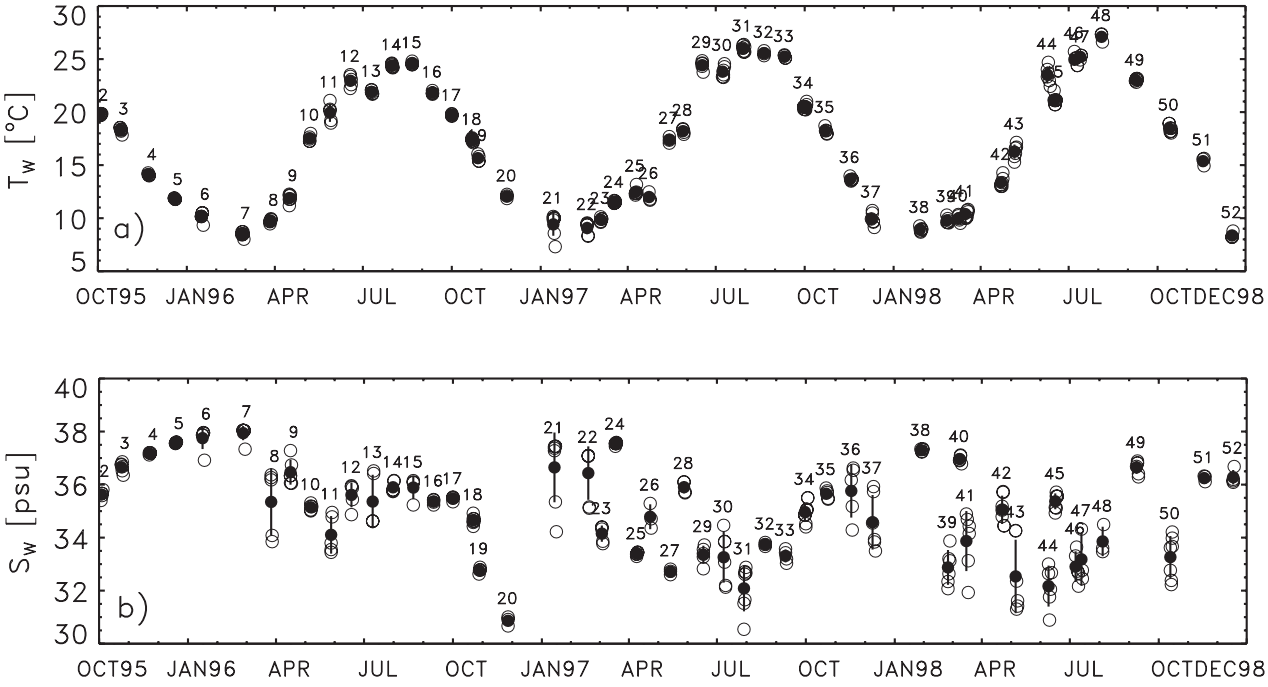

Fig. 1. Time-series of near-surface **a)** temperature, T_w; and **b)** salinity, S_w. For each campaign, the average, the standard deviation around the average, and the individual values are represented by solid circles, a black line, and open circles, respectively. The numbers above the symbols refer to the campaign number.

bottom (the density excess γ can reach values up to 29.4–29.6 characteristic of the northern Adriatic Sea deep waters. Nevertheless, the average salinity profile shows lower values at the surface (a difference of about 1 PSU with respect to the values at 5 m). This inhomogeneity is due to short time scale events showing the presence of a thin (about 2–3 m thick) near-surface layer of low salinity (generally cooler) transported from the north, e.g., campaigns 6 (January 1996), 21 (January 1997), 22 (February 1997), 37 (December 1997), or 39 (February 1998). This fact is also highlighted by the elevated variability (standard deviation) around the average surface value (Fig. 2b).

In the spring (Figs. 2c–d), the increase in the air temperature and the increase in river discharges leads to a more stable stratification (e.g., campaign 8 in late March 1996, or campaign 23 in early April 1997). The thickness of the (homogeneous) near-surface layer remains variable, probably according to the magnitude and duration of wind events. Temperature, in general, progressively decreases from the surface to depth, whereas salinity shows an inverse profile. In summer (Figs. 2e–f), a warm (22.5–26°C at $1\,\sigma$) and low salinity (32.5–36.0 PSU) layer extends from the surface down to about 10 m. At the bottom, temperature and salinity reach 18–22°C and 36.5–37.5 PSU, respectively. Here also, salinity and temperature show markedly opposite vertical profiles. The autumn season (Figs. 2g–h) displays the opposite influence of autumnal river discharges and cooling of the air temperature: salinity and temperature both increase, more or less abruptly, from the surface to depth.

This average or generalized description of the seasonal evolution is in good agreement with the one presented for the whole "Shallow Northern Adriatic" Sea by Zavatarelli et al. (1998).

3.2 Atmospheric Optical Characteristics

CoASTS atmospheric measurements include measurements of the sky radiance in the sun and the almucantar planes, and direct sun irradiance, as well as the ratio of diffuse-to-direct solar irradiance, both continuously measured. The data presented in this section are the aerosol optical thickness, $\tau_a(\lambda)$, where λ is the wavelength, and α is the Ångström exponent. The wavelength dependency of the aerosol optical thickness is commonly expressed by the Ångström law (Ångström 1961) as:

$$\tau_a(\lambda) \;=\; \beta\,\lambda^{-\alpha}, \qquad (1)$$

where β is the Ångström coefficient. The τ_a values were obtained from measurements performed on the tower by a sun photometer included in the Aerosol Robotic Network (AERONET) network (Holben et al. 1998) managed by the National Aeronautics and Space Administration (NASA) Goddard Space Flight Center (GSFC). The τ_a data were screened for clouds by removing any data exceeding the threshold value of 0.1 for $\tau_a(870)$ and then only considering situations for which the relative air mass m was less than or equal to 5. Values of α and β were then computed by least-squares fit of the estimated $\tau_a(\lambda)$ versus λ for the wavelengths 440, 670, and 870 nm.

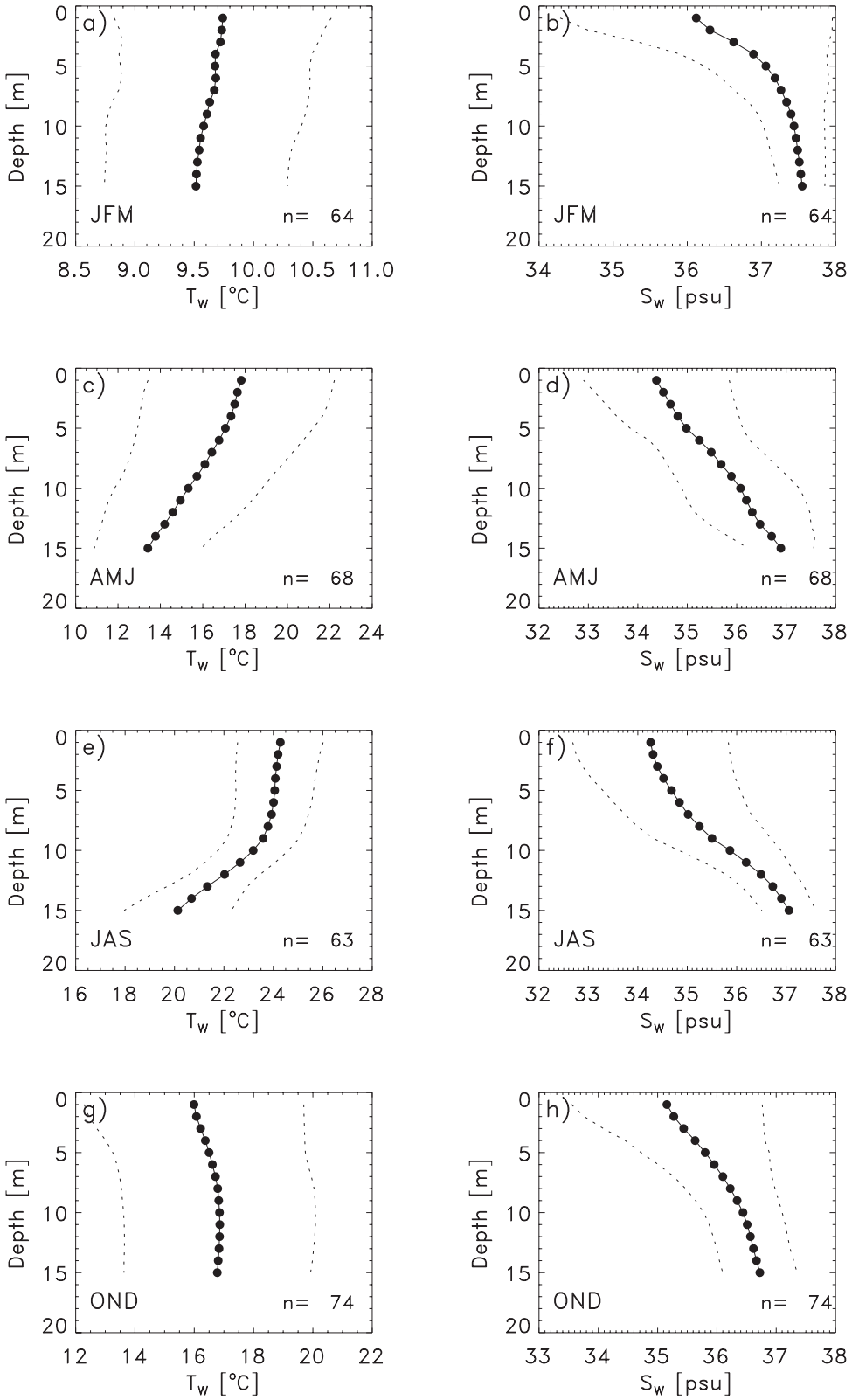

Fig. 2. Average seasonal vertical profiles (1 m binning) of temperature [panels **a)** JFM, **c)** AMJ, **e)** JAS, **g)** OND] and salinity [panels **b)** JFM, **d)** AMJ, **f)** JAS, **h)** OND]. Standard deviations around the average are represented by dotted lines; n refers to the number of stations used for computing the averages.

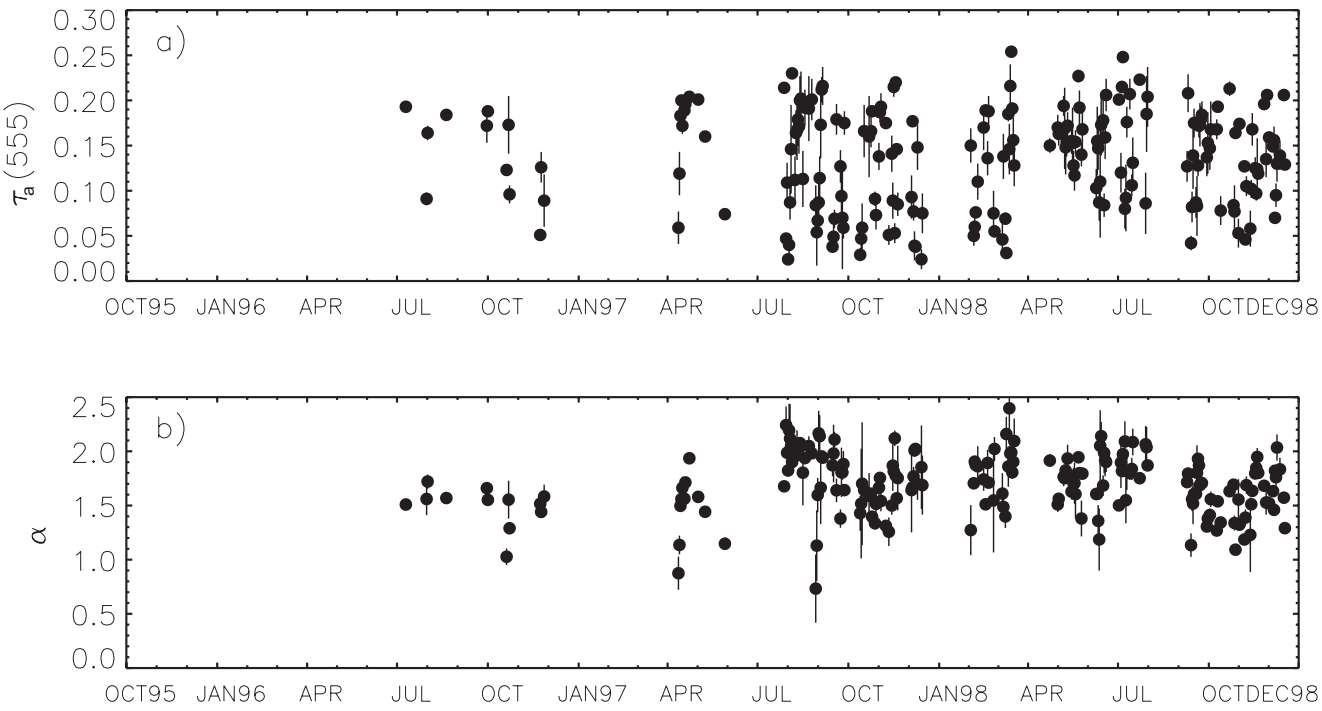

Fig. 3. Time-series of **a)** the aerosol optical thickness τ_a, at 555 nm, and **b)** the Ångström exponent α. Filled circle and black lines represent the daily averages and standard deviations, respectively.

The aerosol optical thickness τ_a at 555 nm (computed using the retrieved values of α and β) and the exponent α, are both shown in Fig. 3 as daily average values together with the associated standard deviation. Values of $\tau_a(555)$ vary in the range of 0.02–0.26 with a global average value of 0.136 ($\sigma = 0.055$).

Standard deviations of daily average values (Fig. 3a), indicate significant short-term variations of the aerosol optical thickness. These can be attributed to short-term changes in the aerosol composition and concentration, due to changes in the local circulation. In Fig. 3b, the exponent α, varies from 0.7–2.4, and shows an average value of 1.70 ($\sigma = 0.27$). These values of α are in agreement with independent measurements performed at different sites in the Po River valley (De Santis et al. 1994) and indicate that small aerosol particles prevail over large particles, thus suggesting a general prevalence of continental aerosol in the measurement area.

3.3 Marine Optical Components

Marine optical components represent the different elements within the water column (including water itself) contributing to the attenuation of light either by absorbing or by scattering photons. Three significant components are classically considered for bio-optical modeling in coastal areas: the pigmented particulate matter (phytoplankton pigments), the nonpigmented particulate matter, and the colored dissolved organic matter—also called "yellow substance"—expressed through its absorption coefficient (presented later in the section on inherent optical properties, Sect. 3.4).

3.3.1 Phytoplankton Pigments

The concentration of phytoplankton pigments (Table 2) was measured by high performance liquid chromatography (HPLC, JGOFS 1994). The total chlorophyll *a* (C_a) concentration for near-surface samples varies from 0.098–8.255 mg m^{-3} with a global average of 1.309 ($\sigma = 1.141$, Table 2). Depth-integrated concentrations (from 1–14 m) vary from 1.7–64.6 mg m^{-2}. In Fig. 4a, a rough seasonal cycle can be observed with a first maximum in February–March (eventually May) and a second one in October–November; minimum values are observed in December–January and June–July. The minima are associated with periods of low vertical stability in December–January, or low nutrient content-stratified waters in summer; whereas the maxima generally correspond to moderately stratified, nutrient-enriched, waters of late winter–spring and autumn (Gilmartin et al. 1990 and Zavatarelli et al. 1998).

Considering the average values for the four seasons (Table 2), the cycle is in agreement with the one defined by Zavatarelli et al. (1998) for the shallow northern Adriatic Sea (north of the Po River delta): maximal in winter and autumn, minimal in summer. Gilmartin and Revelante (1980) observed three different maxima of C_a (fluorimetric method) in January–February, May-June-July, and October–November; however, this observation was made

Table 2. Surface pigment concentrations (in milligrams per cubic meter), including chlorophylls c_1 and c_2, diadinoxanthin, alloxanthin, diatoxanthin, and β-carotenoids—C_{12}, C_D, C_A, C_d, and C_β, respectively—and total suspended matter concentrations, C_{TSM} in grams per cubic meter. The period and statistic notations are the same as in Table 1.

Period	*Stat.*	C_a	C_b	C_{12}	C_F	C_{HB}	C_D	C_A	C_d	C_Z	C_β	C_{TSM}
Global	X_n	268	259	233	267	268	265	259	243	263	249	268
	$\bar{X}$	1.3094	0.0941	0.3005	0.4293	0.2413	0.1151	0.0590	0.0502	0.0877	0.0531	1.081
	X_σ	1.1408	0.1155	0.4468	0.5520	0.1791	0.1238	0.0778	0.0576	0.0944	0.0538	0.695
	X^-	0.098	0.007	0.008	0.008	0.009	0.002	0.002	0.001	0.004	0.002	0.20
	X^+	8.255	0.763	3.022	3.267	1.163	0.720	0.447	0.346	0.608	0.363	5.07
JFM	X_n	64	58	51	64	64	61	60	48	59	59	64
	$\bar{X}$	1.5930	0.1017	0.5837	0.6723	0.2045	0.1384	0.0584	0.0724	0.0283	0.0481	0.992
	X_σ	1.6860	0.0886	0.8419	0.8719	0.1982	0.1616	0.0703	0.0752	0.0128	0.0501	0.530
	X^-	0.098	0.011	0.008	0.008	0.019	0.002	0.002	0.001	0.005	0.003	0.27
	X^+	8.255	0.293	3.022	3.267	1.163	0.670	0.347	0.242	0.062	0.166	2.33
AMJ	X_n	68	68	68	68	68	68	67	65	68	59	68
	$\bar{X}$	1.1494	0.0485	0.2118	0.2795	0.3309	0.1306	0.0516	0.0645	0.0736	0.0459	1.195
	X_σ	0.9553	0.0248	0.1963	0.3686	0.1936	0.1457	0.0451	0.0562	0.0564	0.0435	0.793
	X^-	0.194	0.010	0.016	0.012	0.053	0.007	0.003	0.002	0.004	0.002	0.20
	X^+	4.964	0.101	0.880	1.799	0.925	0.720	0.197	0.236	0.246	0.200	4.13
JAS	X_n	63	60	59	63	63	63	60	63	63	58	62
	$\bar{X}$	0.9278	0.0369	0.1488	0.3055	0.1746	0.0965	0.0166	0.0439	0.1333	0.0538	1.200
	X_σ	0.6172	0.0279	0.0976	0.2789	0.1091	0.084	0.0121	0.0565	0.0861	0.0396	0.940
	X^-	0.186	0.007	0.018	0.035	0.031	0.012	0.003	0.005	0.015	0.004	0.27
	X^+	3.740	0.165	0.563	1.778	0.444	0.513	0.051	0.346	0.414	0.189	5.07
OND	X_n	73	73	55	72	73	73	72	67	73	73	74
	$\bar{X}$	1.5391	0.1774	0.3106	0.4629	0.2477	0.0973	0.1018	0.0265	0.1095	0.0624	0.953
	X_σ	0.9406	0.1691	0.1796	0.4258	0.1636	0.0852	0.1116	0.0300	0.1327	0.0708	0.402
	X^-	0.336	0.007	0.034	0.051	0.009	0.009	0.006	0.002	0.010	0.003	0.27
	X^+	5.163	0.763	0.811	1.807	0.698	0.481	0.447	0.187	0.608	0.363	2.00

within a region of the western part of the northern Adriatic Sea which is mainly influenced by the Po River discharge. Appreciable short time-scale variability adds to the seasonal background.

On several occasions, the value of C_a changed within a campaign (and often within 24 h) by a factor of 2–3 (during October 1995, May 1996, January–February 1997, October–November 1997, May 1998, and October 1998), and up to 8–10 (February–March 1996, and July 1997). This short time-scale variability was often observed in conjunction with a rapid lowering of the near-surface salinity which indicates the southward transport of material from the discharge of northern rivers. In particular, an increase of C_a from 50–850% (computed for pairs of successive stations) were observed during situations of decreasing salinity (a decrease of 0 to −3 PSU). These events can also lead to the observation of C_a maxima in late winter (February or March). Situations of decreasing C_a corresponding to a decrease in salinity, do not lead to a decrease of C_a higher than 50%. On the contrary, incidents of increasing C_a, together with an increase in salinity, were very few and were not found to be significant.

Pigments, particularly the carotenoids, are known to be taxonomic markers of phytoplanktonic populations. The concentration of chlorophyll *b* (C_b), which is an indicator of *Chlorophycea* (green flagellates), shows maximum values in December or January (Fig. 4b), i.e., when the seawater is cold and well mixed. The latter is in agreement with the observation that green flagellates seem to require strong mixing situations to develop (Bustillos-Guzmán et al. 1995). Chlorophyll *b* concentrations can range from 0.007–0.763 mg m^{-3}.

The fucoxanthin concentration (C_F), which is an indicator of the presence of diatom populations, varies from 0.008–3.267 mg m^{-3}. This closely follows the C_a cycle, because the diatom populations are important contributors to the total C_a (Fig. 4c). Diatoms are considered to be very opportunistic; they optimally develop during transition phases between mixed and stratified conditions (Claustre et al. 1994 and Bustillos-Guzmán et al. 1995). Their maxima can, therefore, be observed in spring and autumn. Surface stability and nutrient resources available in some situations (surface transport of lower salinity–nutrient enriched waters) are also favorable to their growth.

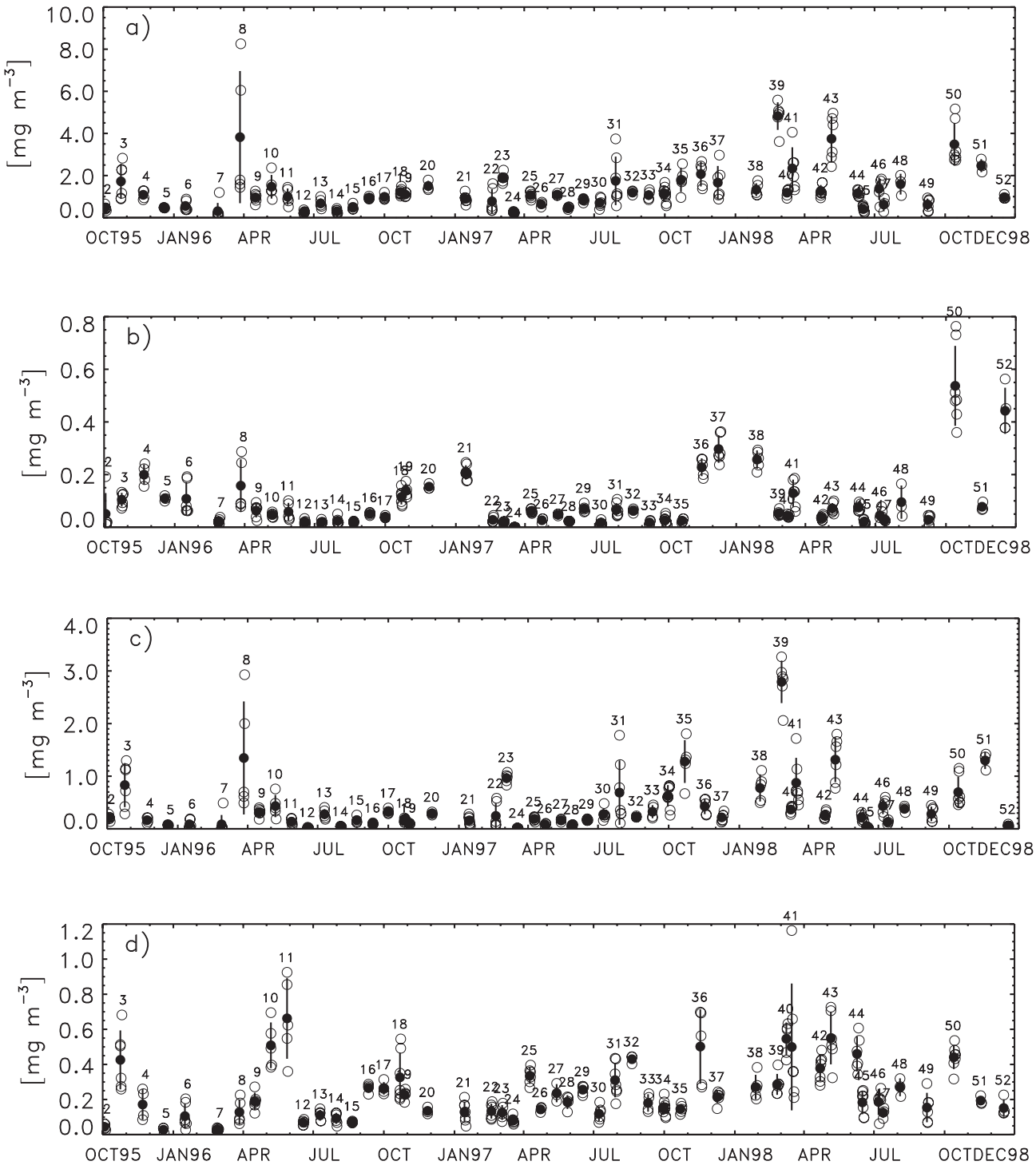

Fig. 4. Time-series of the concentrations of **a)** total chlorophyll *a* (C_a), **b)** chlorophyll *b* (C_b), **c)** fucoxanthin (C_F), and **d)** the sum of the concentrations of 19′-hexanoyloxyfucoxanthin and 19′-butanoyloxyfucoxanthin (C_{HB}). The symbols and lines are the same as presented in Fig. 1. The values represent the average for each campaign.

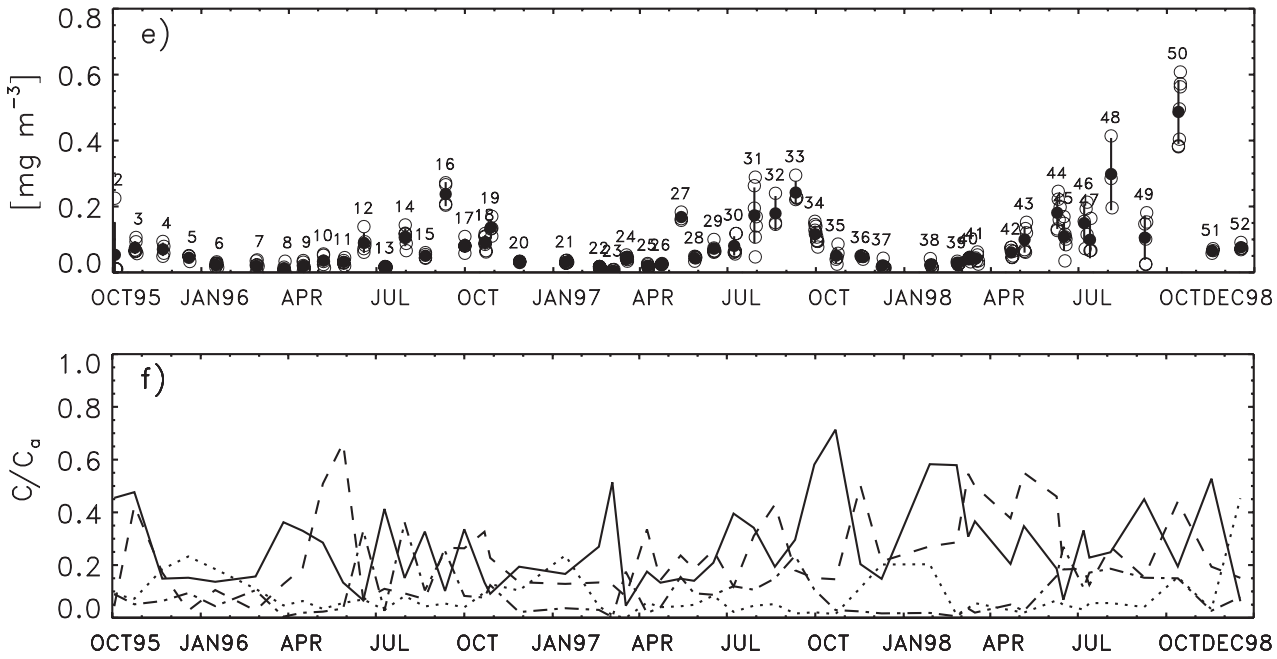

Fig. 4. (cont.) Time-series of the concentrations of **e)** zeaxanthin (C_Z). The symbols and lines are as in Fig. 1. Panel **f)** shows the time-series of the ratio C/C_a where C is the pigment, which in this case is C_b (dotted line), C_F (solid line), C_{HB} (dashed line), and C_Z (dotted and dashed line). The values represent the average for each campaign.

The concentration of 19′-hexanoyloxyfucoxanthin and 19′-butanoyloxyfucoxanthin combined (C_{HB}), which is an indicator of prymnesiophyte and chrysophyte populations, ranges from 0.009–1.163 mg m^{-3} and follows the fucoxanthin cycle with a one month shift (Fig. 4d). These populations are known to be able to adapt to a variety of water column structures (Bustillos-Guzmán et al. 1995).

The zeaxanthin concentration, C_Z (which is an indicator of cyanobacteria and prochlorophyte populations), ranges from 0.004–0.608 mg m^{-3}. The seasonal variations of C_Z clearly show a shift in time with respect to fucoxanthin concentrations, and are almost perfectly opposite to the C_b cycle, with a very distinct maximum in August–September when the water is thermally stratified, and a minimum in January–February when the water is cold and well mixed (Fig. 4e). This global succession can be highlighted by the C:C_a ratios (Fig. 4f):

- The C_b:C_a ratio reaches maximum values of 0.2–0.4 in winter;
- The C_F:C_a ratio reaches values of about 0.4–0.7 in March–April or October–November;
- The C_{HB}:C_a reaches values of 0.35–0.65 mainly in April–May or November; and
- The C_Z:C_a ratio reaches values of 0.25–0.35 in June–July–August.

This temporal succession is in agreement with previous analyses reported in the literature, particularly for the Mediterranean Sea (e.g., Bustillos-Guzmán et al. 1995). Concentrations of the other measured pigments can be found in Table 2.

3.3.2 Total Suspended Matter

The concentration of total suspended matter, C_{TSM}, was measured according to Strickland and Parson (1972). Values ranged from 0.20–5.07 g m^{-3} with a global average of 1.081 (σ=0.695), as shown in Table 2. The basic seasonal cycle of C_{TSM} (Fig. 5a) shows maxima in April–May and October–November and minimum in January. Nevertheless, the second minimum observed in July–August for C_a is not as well evidenced here. The short time-scale variability characterizing C_a also affected the C_{TSM} distribution near the surface: a decrease in salinity of −0.5 to −2.5 PSU was related to a C_{TSM} increase of from 100–700%. Such events were particularly important during the summers of 1997 and 1998, and led to a global average summer concentration equivalent to the one in the spring but with a higher standard deviation (Table 2). It should be noted that the concentrations from summer 1997 (in particular, campaign numbers 30 and 31) were affected by the presence of high quantities of suspended mucus material as part of a so-called *mucilage* event, which occurred in the northern Adriatic Sea at that time (Berthon et al. 2000).

3.3.3 Size Distribution of Particles

The size distribution of particles was measured using the Coulter Counter technique for the range 1.8–64 μm.

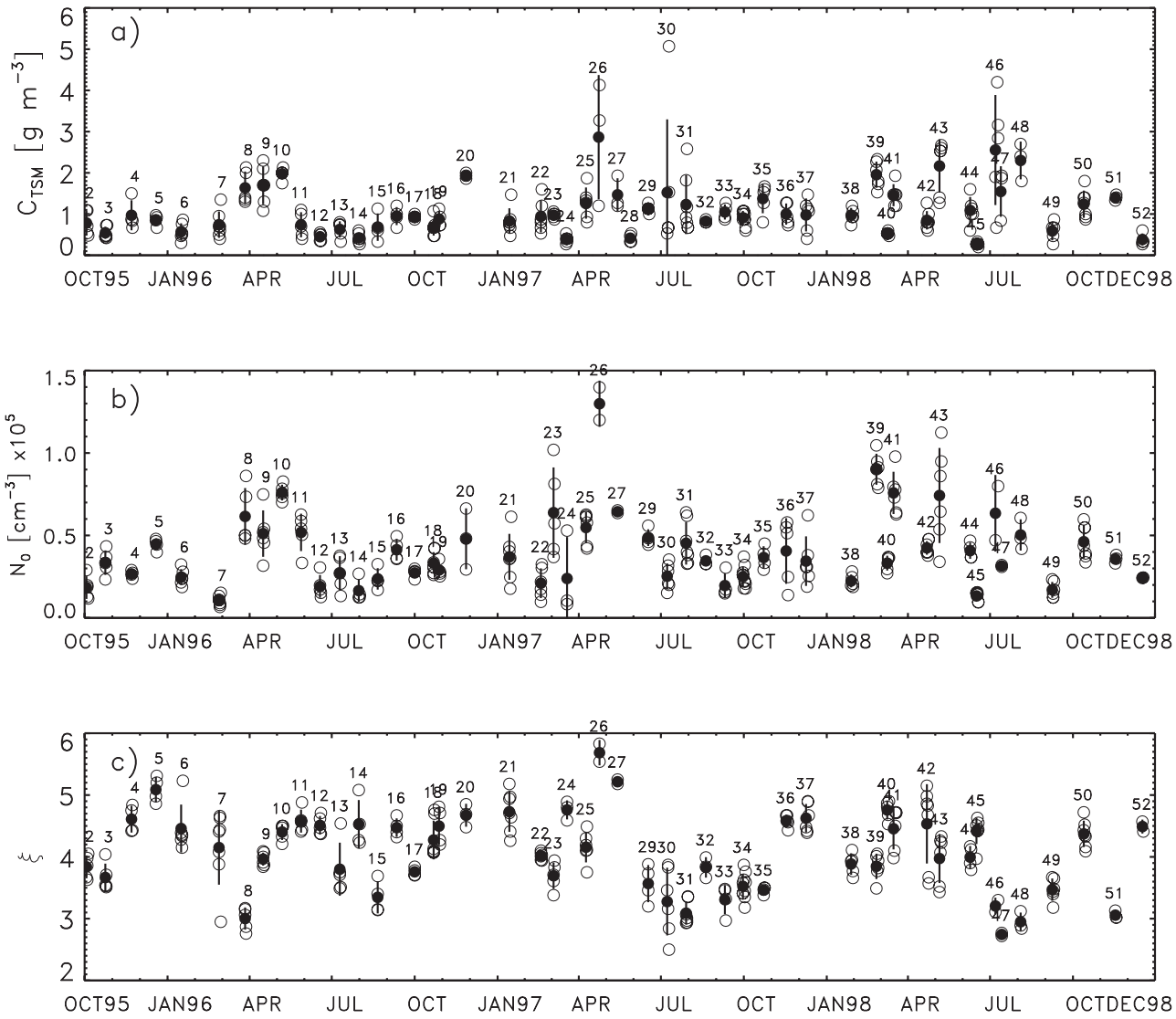

Fig. 5. Time-series of **a)** total suspended matter concentration (C_{TSM}), **b)** concentration of particles, N_0, from 2–30 μm, and **c)** the coefficient ξ of the Junge power law. The symbols and lines are as in Fig. 1.

Figures 5b and 5c present the time series of the concentration of particles, N_0 (in units of per cubic centimeters) with diameters ranging from 2–30 μm and of the exponent ξ of the Junge-type power function (Junge 1963) fitted using the least-squares method to the measured size distribution of particles:

$$N = kD^{-\xi}, \tag{2}$$

where N is the number of particles of diameter D, and k is the Junge coefficient.

The concentration of particles, N_0 (Fig. 5b), is well correlated with C_{TSM}, although a part of the measured C_{TSM} (0.7-2.0 μm) is not included in the present size distribution of particles. Values of ξ (Fig. 5c) range from 2.5–5.8 with an average of 4.06 ($\sigma = 0.62$). Such a function does not always adequately represent the measured size spectra, and probably causes some of the high variability in ξ values observed for individual campaigns. Nevertheless, the use of this power function has ensured a first synthesis of the particle size distribution measurements. The derived high average value of ξ is close to the one compiled by Jonasz (1983) for the Mediterranean Sea. The link between ξ and the *in situ* attenuation and scattering coefficients will be discussed below.

3.3.4 Vertical Distribution

In the analyses presented above, as well as in those given later in this document, predominantly near-surface values were considered. The average seasonal profiles of temperature and salinity (Fig. 2) showed that the highest variability occurred within the near-surface layer (about 0–5 m) in particular, because of the rapid passage of less salty water. Figure 6 shows the corresponding seasonal average vertical profiles of C_a and C_{TSM}. Two situations are

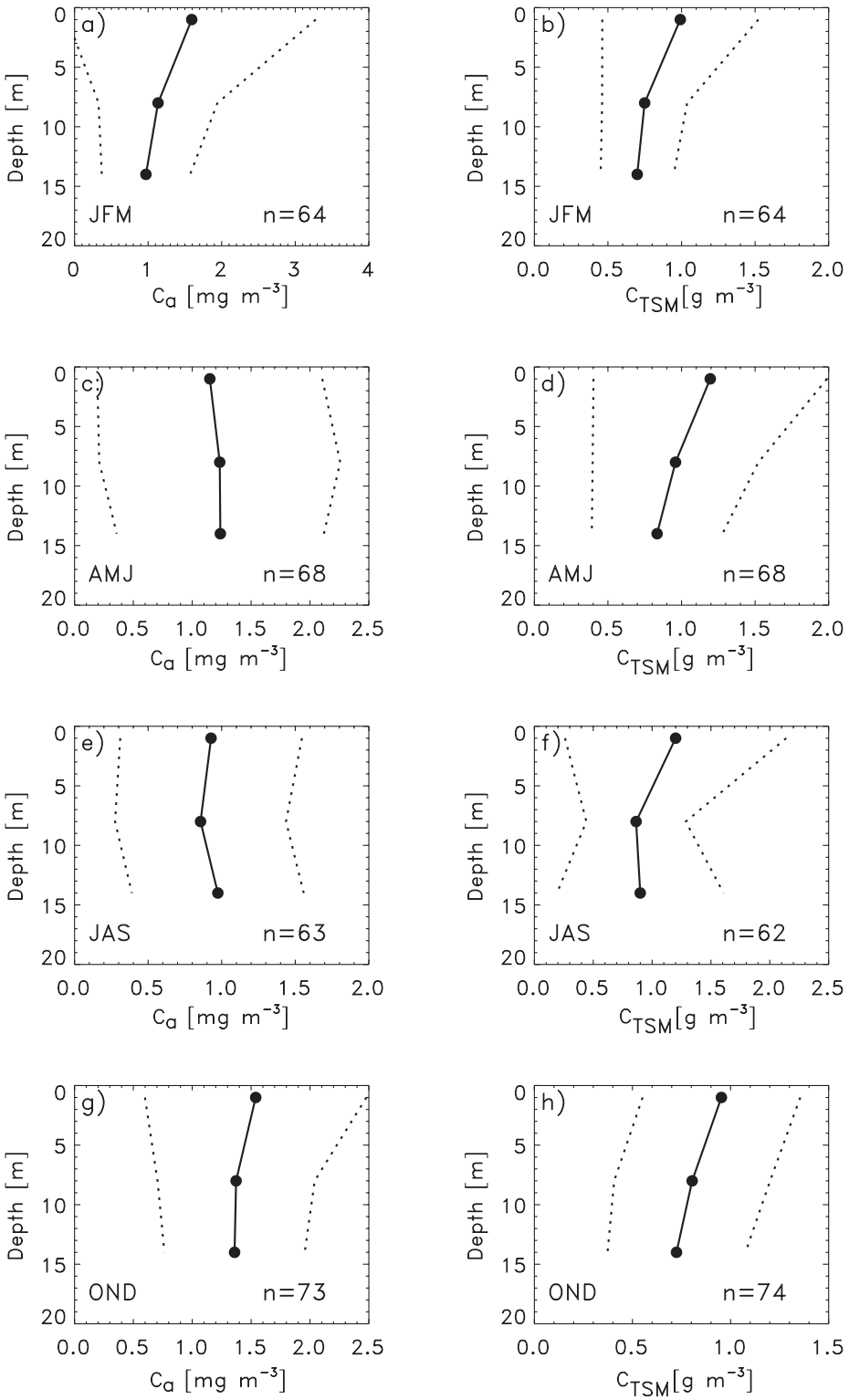

Fig. 6. Average seasonal vertical profiles of C_a, **a)** JFM, **c)** AMJ, **e)** JAS, and **g)** OND; and C_{TSM}, **b)** JFM, **d)** AMJ, **f)** JAS, and **h)** OND. The values are computed from the samples taken at three discrete depths (near-surface, 8 m, and 14 m). Standard deviations around the average are represented by dotted lines.

observed: 1) a rather homogeneous profile (e.g., spring or summer for C_a); and 2) stratification at the surface (e.g., winter for C_a and C_{TSM}). As seen with temperature and salinity, the near-surface layer shows the greatest variability. Note that the shape of the C_{TSM} profile (and to a lesser extent the C_a profile) is inversely correlated with respect to the average salinity vertical profile.

The present vertical distributions of C_a are in rather good agreement with the average seasonal distributions presented by Zavaterelli et al. (1998) for the shallow northern Adriatic Sea (north of the Po River estuary), although their values for the winter season were somewhat higher (average near-surface values of $2.7\,\mathrm{mg\,m^{-3}}$). In addition, the vertical profiles of the beam attenuation and absorption coefficients (obtained from AC-9 measurements) demonstrated that in almost all situations, the sampling at the three fixed depths (near-surface, 8 m, and 14 m) did not miss any particular aspect of the subsurface structure.

3.4 Marine Inherent Optical Properties

This section describes the variations of the measured inherent optical properties: *in vivo* absorption coefficients measured on filtered seawater samples, *in situ* absorption, and scattering coefficients estimated from the AC-9 measurements.

3.4.1 *In Vivo* Absorption

Spectra of the *in vivo* absorption coefficient of total and nonpigmented particulate matter, $a_p(\lambda)$ and $a_{dp}(\lambda)$, respectively, were measured within the range of 400–750 nm with a 1 nm resolution according to Tassan and Ferrari (1995) on the water samples collected at discrete depths. The difference of $a_p(\lambda) - a_{dp}(\lambda)$ gives the absorption coefficient of pigmented matter, $a_{ph}(\lambda)$. The absorption coefficient spectrum of colored dissolved organic matter, i.e., yellow substance, $a_{ys}(\lambda)$, was measured within the interval 350–750 nm according to Ferrari et al. (1996). The spectra $a_{ph}(\lambda)$, $a_{dp}(\lambda)$, and $a_{ys}(\lambda)$ are presented for the near-surface samples in Fig. 7 through their values at 443, 400, and 400 nm, respectively (statistics are given in Table 3). The values presented for $a_{dp}(\lambda)$ and $a_{ys}(\lambda)$ at 400 nm actually are the a_0 values resulting from the following exponential law fitted to each spectra (for the range 400–650 nm for a_{dp} and 350–600 nm for a_{ys}):

$$a_{xx}(\lambda) \;=\; a_{0xx}\,\exp[-S_{xx}(\lambda-\lambda_0)] \;+\; cb_{xx}, \qquad (3)$$

where xx is either dp or ys; a_{0xx}, S_{xx}, and cb_{xx} are the coefficient, slope, and background of the exponential law, respectively; and λ_0 is the reference wavelength (i.e., 400 and 350 nm for dp and ys, respectively).

The presence of cb_{xx} in the fitting function deserves additional comment. Concerning $a_{ys}(\lambda)$, it is well known that absorption in the red end of the spectrum is negligible (Kirk 1994). Measured absorption in this spectral range has been interpreted as a residual due to scattering by very small particles which passed through the ($0.22\,\mu$m) filter, formed in the cuvette before the measurements (e.g., colloids), or as a result of a difference in the refractive index between the sample and the reference due to a difference in salinity (Green and Blough 1994). In the results presented here, however, the background cb_{ys} exhibited an appreciable variability for sampled water with the same salinity, therefore not supporting the Green and Blough (1994) hypothesis. On the contrary, a rough correlation between cb_{ys} and $a_{ys}(\lambda)$ was observed, which supports the scattering hypothesis. A constant background implicitly assumes scattering by submicron particles is not wavelength dependent, but this was chosen as such for the sake of simplicity.

The same hypothesis of a null $a_{dp}(750)$ value is not as well grounded, especially for inorganic particles. Nevertheless, the general approach (Mitchell and Kiefer 1988) consists of subtracting the value measured at 750 nm from the whole spectra before fitting it to the exponential law. After several trials, (3) was found to give the best fit for the a_{dp} spectra. In particular, it helped account for a change of slope frequently observed in the spectral domain 550–600 nm. Statistics on S_{xx} and cb_{xx} are given in Table 3.

The $a_{ph}(443)$ values range from 0.009–$0.295\,\mathrm{m^{-1}}$ with an average of $0.0569\,\mathrm{m^{-1}}$ ($\sigma = 0.0391$). As expected, the variations of $a_{ph}(443)$ closely followed the evolution of C_a at seasonal (with spring and autumn maxima, winter and summer minima) and campaign time scales (Fig. 7a). The C_a specific-absorption coefficient of the pigmented particulate matter, a^*_{ph} at 443 nm varies from 0.018–$0.141\,\mathrm{m^2\,mg^{-1}}$ of C_a, i.e., by about a factor of 8, with an average of 0.0506 (σ=0.0175). Its seasonal variation (Fig. 7b) is inversely distributed compared to $a_{ph}(443)$ because $a^*_{ph}(\lambda)$ decreases when C_a increases (e.g., Bricaud et al. 1995). Fig. 7e also presents the ratio $a_{ph}(\lambda)$:$a_{ph}(443)$ for different SeaWiFS wavelengths. Variations of the presented ratios are rather limited. Roughly, low values of both ratios $a_{ph}(550)$:$a_{ph}(443)$ and $a_{ph}(665)$:$a_{ph}(443)$ are associated with high values of $a_{ph}(488)$:$a_{ph}(443)$ and vice-versa. Minimum values for the two first ratios may indicate a flattening of the absorption spectra due to the package effect (Morel and Bricaud 1981). In effect, minimal values of $a^*_{ph}(443)$ are generally (but not systematically) observed in conjunction with these low ratios. The ratio $a_{ph}(412)$:$a_{ph}(443)$ shows some peaks with values higher than 1 probably due to high concentrations of phaeopigments (however this has not been confirmed by the HPLC measurements).

The *fitted* $a_{dp}(400)$ values range from 0.005–$0.312\,\mathrm{m^{-1}}$ with an average of $0.0481\,\mathrm{m^{-1}}$ ($\sigma = 0.0318$), whereas the average background cb_{dp} value is $0.007\,\mathrm{m^{-1}}$, i.e., about 15% of the average $a_{dp}(400)$ value. The seasonal evolution of $a_{dp}(400)$ (Fig. 7c) roughly follows that of $a_{ph}(443)$ (the plot of the one versus the other—not shown here—nevertheless exhibits a considerable scattering) and follows quite well the evolution of the C_{TSM} concentration

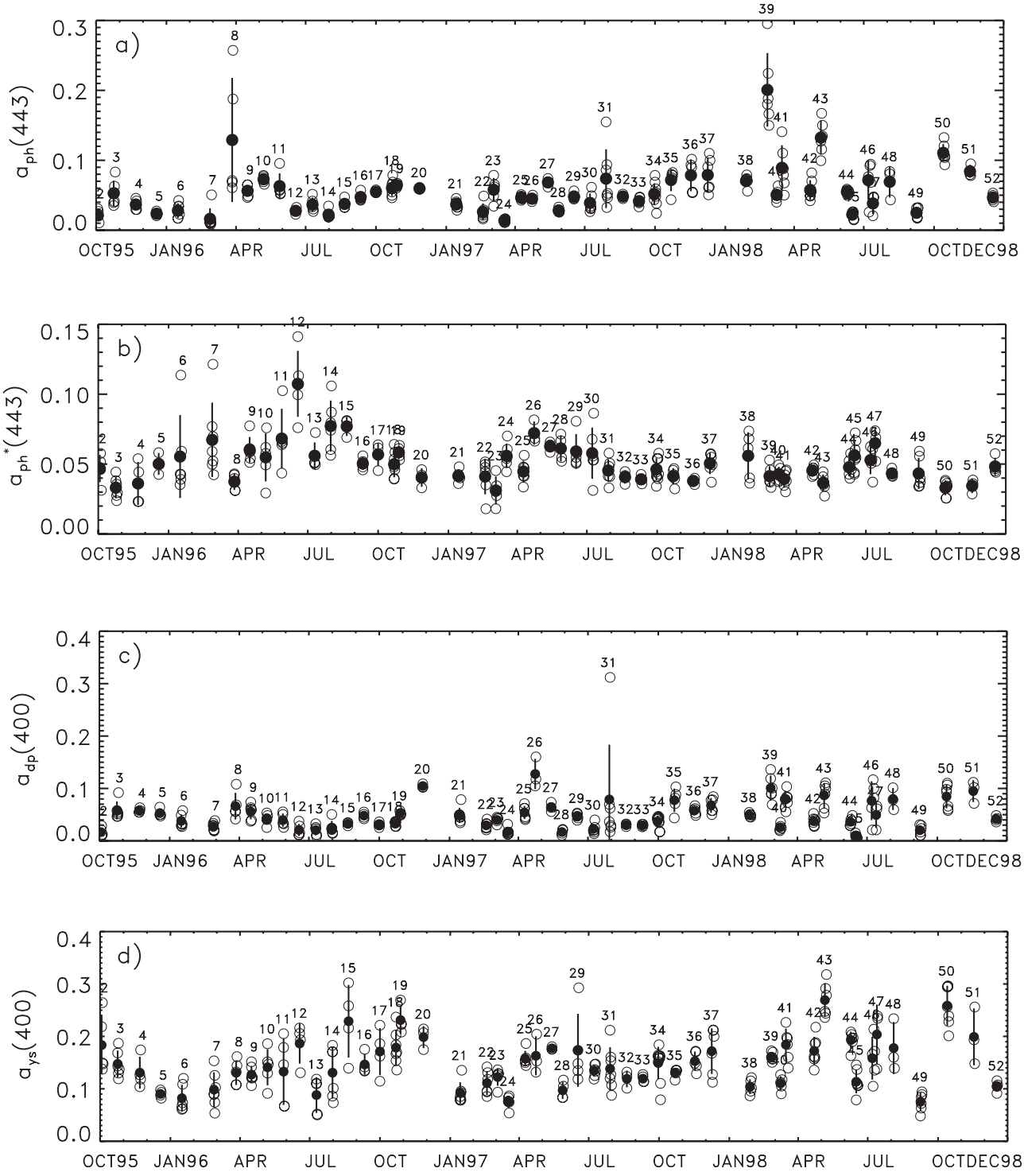

Fig. 7. Time series, for near-surface samples, of **a)** the absorption coefficient of pigmented particulate matter a_{ph}, at 443 nm in per unit meters; **b)** the corresponding chlorophyll *a*-specific absorption coefficient $a^{*}_{ph}(443)$ in meters square per milligram of chlorophyll *a*; **c)** the absorption coefficient of nonpigmented particulate matter a_{dp} at 400 nm in per unit meters; and **d)** the absorption coefficient of colored dissolved organic matter a_{ys}, at 400 nm in per unit meters. The symbols and lines are as in Fig. 1.

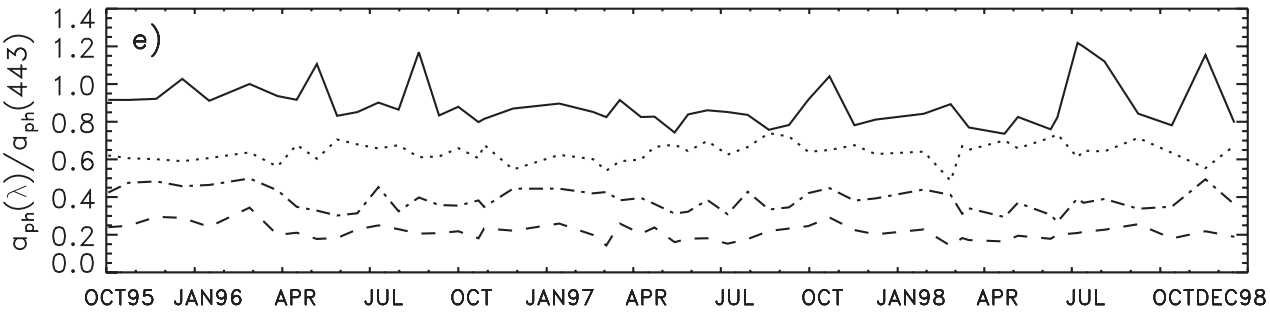

Fig. 7. (cont.) Panel **e)** shows the time series of the ratio $a_{ph}(\lambda)/a_{ph}(443)$ for $\lambda = 412$ (solid line), 488 (dotted line), 510 (dashed line), and 665 (dotted and dashed line). The values correspond to the averages of each campaign.

Table 3. Surface absorption coefficients, in units of per meter, of pigmented (a_{ph}) and nonpigmented (a_{dp}) particulate matter and of colored dissolved organic matter (a_{ys}) at 443, 400, and 400 nm, respectively. Parameter (S_{xx} and cb_{xx}) of the exponential curve fitted to the a_{dp} and a_{ys} spectra (see text). The period and statistic notations are the same as in Table 1.

Period	*Statistic*	$a_{ph}(443)$	$a_{dp}(400)$	S_{dp}	cb_{dp}	$a_{ys}(400)$	S_{ys}	cb_{ys}
Global	X_n	268	268	268	268	268	268	268
	$\bar{X}$	0.05685	0.04807	0.0119	0.00708	0.14906	0.0181	0.02605
	X_σ	0.03905	0.03177	0.0014	0.00464	0.05615	0.0023	0.03441
	X^-	0.0085	0.0054	0.008	−0.0005	0.0482	0.011	−0.0343
	X^+	0.2954	0.3119	0.017	0.0375	0.3733	0.028	0.1969
JFM	X_n	64	64	64	64	64	64	64
	$\bar{X}$	0.06340	0.04734	0.0113	0.00754	0.11491	0.0170	0.02009
	X_σ	0.06255	0.02768	0.0014	0.00401	0.03797	0.0019	0.03200
	X^-	0.0085	0.0123	0.008	0.0000	0.0536	0.011	−0.0125
	X^+	0.2954	0.1362	0.015	0.0190	0.2266	0.021	0.1603
AMJ	X_n	68	68	68	68	67	67	67
	$\bar{X}$	0.05601	0.04579	0.0126	0.00746	0.16232	0.0190	0.02794
	X_σ	0.02987	0.02960	0.0013	0.00556	0.05380	0.0021	0.03523
	X^-	0.0147	0.0054	0.010	0.0000	0.0666	0.013	−0.0343
	X^+	0.1671	0.1602	0.017	0.0297	0.3180	0.026	0.1969
JAS	X_n	62	62	62	62	63	63	63
	$\bar{X}$	0.04545	0.04216	0.0121	0.00618	0.14741	0.0190	0.03002
	X_σ	0.02428	0.04183	0.0010	0.00574	0.06186	0.0029	0.03326
	X^-	0.0170	0.0090	0.009	−0.0005	0.0482	0.013	−0.0116
	X^+	0.1549	0.3119	0.015	0.0375	0.3733	0.028	0.1643
OND	X_n	74	74	74	74	74	74	74
	$\bar{X}$	0.06153	0.05576	0.0115	0.00709	0.16798	0.0176	0.02613
	X_σ	0.02683	0.02588	0.0013	0.00285	0.05358	0.0016	0.03656
	X^-	0.0105	0.0098	0.008	0.0021	0.0791	0.013	−0.0256
	X^+	0.1325	0.1117	0.014	0.0144	0.2964	0.022	0.1664

in Fig. 5a. The slope S_{dp} varies from 0.008–0.017 with an average of 0.0119 ($\sigma = 0.0014$), and the amplitude of the seasonal variations are lower than for a_{dp} (Table 3). The slope S_{dp} does not exhibit any particular correlation with a_{dp}.

The $a_{ys}(400)$ values vary from 0.05–0.30 m^{-1} with a global average of 0.142 m^{-1} ($\sigma = 0.051$) (Table 3). Here too, a global cycle with winter and summer minima and spring and autumn maxima can be identified although it is less evident for the period of April 1996–September 1996 (Fig. 7d). The slope S_{ys} in (3), resulting from the fit within the interval 350–600 nm, shows an average value of 0.0180 ($\sigma = 0.0024$). The resulting average background value cb_{ys} is about 17% of the average $a_{ys}(400)$ value. This background may occasionally show negative values (minimum values in Table 3) that remain within the noise level.

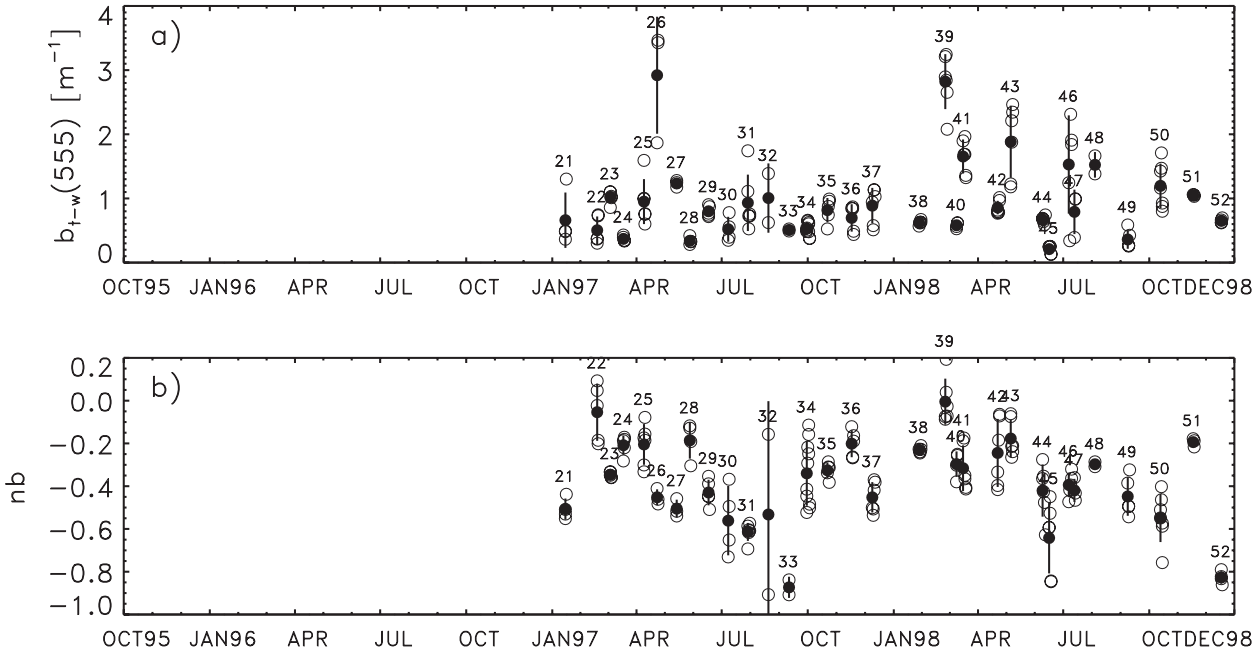

Fig. 8. Time-series of **a)** the near-surface total (except water) scattering coefficient $b_{t-w}(\lambda)$ at 555 nm (average value for a 1 m layer); and **b)** the coefficient nb of the power function describing $b_{t-w}(\lambda)$ spectral dependency (see text). The symbols and lines are as in Fig. 1.

3.4.2 *In Situ* Absorption and Scattering

In situ vertical profiles of total (except water) spectral beam attenuation and absorption coefficients, $c_{t-w}(\lambda)$ and $a_{t-w}(\lambda)$, respectively, at the nominal wavelengths 412, 440, 488, 510, 555, 630, 650, 676, and 715 nm, were measured with an AC-9 (Wetlabs, Inc.). The difference of $c_{t-w}(\lambda) - a_{t-w}(\lambda)$ gives the (non-water) spectral scattering coefficient $b_{t-w}(\lambda)$. The AC-9 deployments only started during campaign 21 (January 1997).

In Zibordi et al. (2002), it was shown that the agreement between $a_{t-w}(\lambda)$, corrected for scattering using Zaneveld et al. (1992), and the sum of the *in vivo* absorption coefficients of the three components described above $[a_{ph}(\lambda)+a_{dp}(\lambda)+a_{ys}(\lambda)]$ is reasonably good. This is particularly true for the blue part of the spectrum, although the spreading of the points is rather high. Figure 8 presents the time series of $b_{t-w}(\lambda)$ at 555 nm, i.e., $c_{t-w}(555) - a_{t-w}(555)$ near the surface (average value within the 0.5–1.5 m near-surface layer), together with the exponent nb of the power function describing its spectral dependence. This exponent was obtained by fitting each $b_{t-w}(\lambda)$ spectra within the interval 412–650 nm, to the following relationship

$$b_{t-w}(\lambda) \; = \; b_{t-w}(\lambda_0)[\lambda/\lambda_0]^{nb}, \qquad (4)$$

where $\lambda_0 = 555$ nm. Quality control of the fit was performed by rejecting situations with a χ^2 value exceeding a fixed threshold (1.10^{-3}).

Values of $b_{t-w}(555)$ vary from 0.1–3.5 m^{-1} (Fig. 8a) with an average value of 0.96 m^{-1} ($\sigma = 0.68$). Variations of $b_{t-w}(555)$ are related to those of $C_{\rm TSM}$ (Fig. 5a) and of the concentration of particles N_0 (Fig. 5b). The values of the exponent nb shown in Fig. 8b vary from -0.9 to $+0.2$ (actually, very few values are positive) with an average of -0.37 ($\sigma = 0.21$). An approximate cycle can be identified with high values generally observed in the winter–spring period and lower ones in summer (this was true primarily for 1997). It is generally accepted that the spectra of the scattering coefficient become less flat as the particle populations are dominated by small particles (Stramski and Kiefer 1991). In winter–spring, the living particles are probably dominated by diatoms (this also corresponds to the period when river discharge may have a major influence); whereas in summer, small species (e.g., cyanobacteria) are predominant, as observed in the pigment succession presented in Sect. 3.3.1.

Suspensions having a size distribution described by the Junge power law show a spectral dependence of the beam attenuation coefficient $c(\lambda)$ proportional to $\lambda^{3-\xi}$, with ξ being the exponent of the Junge law (Diehl and Haardt 1980, and Reuter 1980). In the present situation, the average value of 4.06 for ξ would yield an average dependence of $c_{t-w}(\lambda)$ proportional to $\lambda^{3-4.06} = \lambda^{-1.06}$. When directly computed on measured individual $c_{t-w}(\lambda)$ spectra within the interval of 412–650 nm, an average dependence with $\lambda^{-0.81(\pm 0.23)}$ was found. The value of the exponent lays between the typical -1 assumed for oceanic waters by Loisel and Morel (1998) and the mean -0.5 proposed by Voss (1992) for a wide range of oceanic and coastal locations. It also has to be recalled that the measured

size distributions were limited to 2 μm at the lower end of the diameter range and that many of them were not fully following the Junge law. According to Diehl and Haardt (1980) the expression $c(\lambda) \propto \lambda^{3-\xi}$ can also be applied to the wavelength dependence of the scattering coefficient. Nevertheless, as shown above, the spectral dependence of $b_{t-w}(\lambda)$ computed here is $\lambda^{-0.37(\pm 0.21)}$, suggesting an appreciable effect of $a_{t-w}(\lambda)$ (particularly in the blue part of the spectrum) in the resulting average spectral dependence of $c_{t-w}(\lambda)$.

Linear relationships relating $b_{t-w}(\lambda)$ and $b_{t-w}(555)$, as presented by Gould et al. (1999), were also investigated. The resulting slopes were close to those proposed by these authors, e.g., 1.063 at 412 nm and 0.869 at 676 nm versus 1.160 and 0.850, respectively, given in Gould et al. (1999). Note that in this last analysis, the scattering contribution by *pure* water was included in the total scattering coefficient, $b(\lambda)$.

3.5 Marine Apparent Optical Properties

The marine apparent optical properties are derived from measured profiles of downward spectral irradiance $E_d(z,\lambda)$, upwelling spectral radiance $L_u(z,\lambda)$, and upward irradiance $E_u(z,\lambda)$. All the data are collected at the nominal center wavelengths of 412, 443, 490, 510, 555, 665, and 683 nm using Satlantic ocean color irradiance- and radiance series-200 (OCI-200 and OCR-200, respectively) radiometers. There are four variables derived from these measurements that are of particular interest:

1) The diffuse attenuation coefficient for downward irradiance, $K_{E_d}(\lambda)$, computed for an optically homogenous near-surface layer (Zibordi et al. 2002), for which the minimum and maximum depths were typically 0.3 and 4.5 m, respectively;
2) The subsurface ($z = 0^-$) remote sensing reflectance $R_{\rm rs}(0^-,\lambda) = L_u(0^-,\lambda)/E_d(0^-,\lambda)$ and irradiance reflectance $R(0^-,\lambda) = E_u(0^-,\lambda)/E_d(0^-,\lambda)$;
3) The factor of non-isotropy of the light field measured at nadir, $Q_n(0^-,\lambda) = E_u(0^-,\lambda)/L_u(0^-,\lambda)$; and
4) The normalized water-leaving radiance, $L_{WN}(\lambda)$.

As described in Zibordi et al. (2002), optical measurements and the resulting apparent optical properties were corrected for bottom effects (Maritorena et al. 1994), instrument self-shading (Zibordi and Ferrari 1995) and tower shading (Doyle and Zibordi 2002). A quality control procedure was performed on the data by eliminating the stations for which any of the following were determined to be applicable:

a. The ratio of diffuse to direct above-water downward irradiance was greater than 2 (in order to reject measurements not made under clear-sun† conditions);
b. The relative difference of the irradiance reflectance (at 0^- depth) between two successive casts of the same station was greater than 10% (in order to reject measurements made in unstable‡ environmental conditions); or
c. The $K_{E_d}(\lambda)$ spectral values computed for the near-surface layer were lower than the values measured by Smith and Baker (1978) for the clear waters of the Sargasso Sea.

As a consequence, the number of optical stations used in the following analysis is reduced with respect to the precedent series.

Figure 9 gives the time series of $K_{E_d}(555)$, $Q_n(0^-,555)$, and the ratio $R(0^-,490)/R(0^-,555)$. From this point on, the depth argument $z = 0^-$ is omitted for the sake of simplicity. The presentation and discussion on apparent properties will be further developed in Sect. 4 which relates the seawater optical components and their associated inherent optical properties to the apparent optical properties.

Figure 9a shows the diffuse attenuation coefficient for downward irradiance, K_{E_d} at 555 nm, which varies from 0.08–0.37 $\rm m^{-1}$, and has an average value of 0.180 $\rm m^{-1}$ (σ=0.059). The tendency previously described for the optical components (minimum in December–January and maximum in March–April, as well as October–November) is roughly reproduced here for the years 1996 and 1997, however, the year 1998 is much less defined. The $K_{E_d}(555)$ values are well correlated with the $C_{\rm TSM}$ concentrations, but neither parameter exhibited a well-defined cycle during the year 1998 (Fig. 5a).

The Q_n values at 555 nm show amplitudes ranging from 3.9–6.2 sr with an average value of 4.87 (σ=0.49), which are in agreement with the theoretical studies of Morel and Gentili (1996). The temporal evolution of Q_n shows almost regular large variations overlapped by relatively small short-term variations (Fig. 9b). The large variations, exhibiting a maximum in winter and a minimum in summer, are mainly attributed to seasonal changes of the average solar zenith angle. The short-term variations, within campaigns, are attributed to changes in the water optical properties and in the illumination conditions (variations of the sun zenith, aerosol content, cloudiness, etc.) from station to station.

The analyses of Q_n spectra also show a significant dependence with wavelength. The results exhibit higher values of Q_n at wavelengths characterized by higher absorption of seawater, mostly in the red part of the spectrum. In

† Refer to Zibordi et al. (2002) for an in-depth discussion of the definition of clear-sun and clear-sky conditions, and the differences between the two.

‡ Principally those data affected by illumination changes, sea state effects, etc., and as further explained in Zibordi et al. (2002).

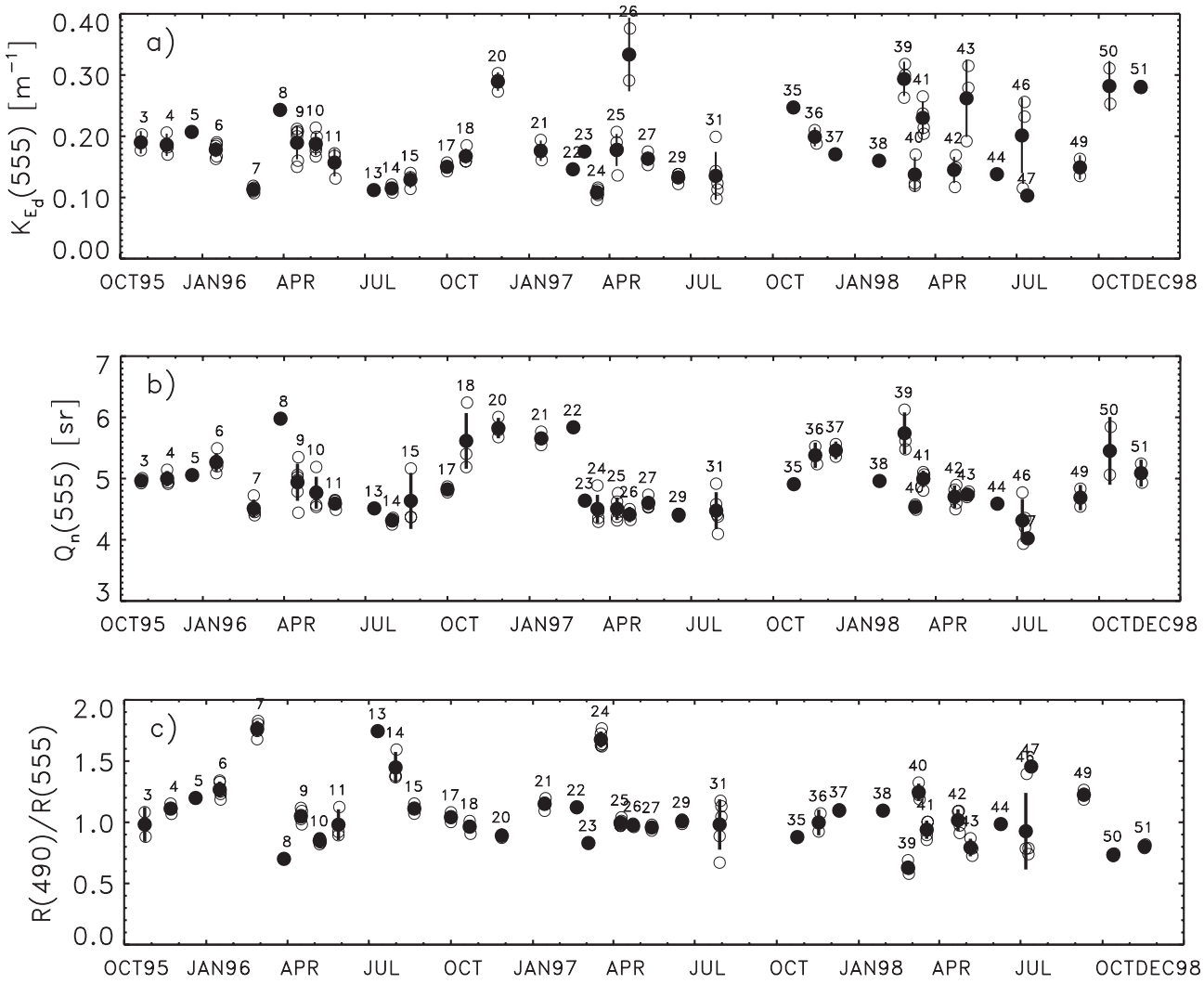

Fig. 9. The time-series' of **a)** $K_{E_d}(555)$ computed for an optically homogeneous near-surface layer; **b)** the surface (0^-) Q_n factor at 555 nm, and **c)** the surface (0^-) reflectance ratio $R(490)/R(555)$. The symbols and lines are as in Fig. 1.

the spectral range 412–665 nm, the highest average value (i.e., 5.56 with σ=0.99) and the highest annual variations (i.e., ranging from approximately 4.0–8.2) have both been observed at 665 nm. A more detailed analysis on the Q-factor dependence with the sun geometry and the optical properties of the seawater is given in Zibordi and Berthon (2001).

Figure 9c presents the time series of the irradiance reflectance ratio $R(490)/R(555)$. The two wavelengths for this ratio are classically coupled when trying to empirically relate reflectance or normalized water-leaving radiance ratios to the chlorophyll a concentration in the open ocean (e.g., O'Reilly et al. 1998 and Kahru and Mitchell 1999). Values of this ratio encompass a rather limited range, from 0.5–2.0, with an average value of 1.08 (σ=0.27). The variability within individual campaigns is small compared to the previously studied quantities. It can clearly be seen that $R(490)/R(555)$ is inversely correlated with $K_{E_d}(555)$ shown in Fig. 9a. The presentation of relationships between reflectance ratios and optical components will be made in the following sections.

4. DISCUSSION

In this section, the bio-optical status of the site (i.e., its classification according to Case-1 or Case-2 types) is discussed and empirical algorithms for chlorophyll a and total suspended matter retrieval from marine reflectance, are presented.

4.1 Case-1 and Case-2 Waters

The Case-1 water corresponds to water for which the optical properties are only determined by the phytoplankton and its derivative products (Morel and Prieur 1977).

On the contrary, the optical properties of the Case-2 waters are also determined by other material (from terrestrial- or bottom origin for example) not systematically co-varying with the phytoplanktonic components.

In the present study, the discrimination between Case-1 and Case-2 water types is based on the recent work of Loisel and Morel (1998), who revisited the relationship between C_a and the total (except water) beam attenuation coefficient at 660 nm, $c_{t-w}(660)$. Here, the values of $c_{t-w}(660)$ have not been directly measured—they have been extrapolated from the measurements at 670 nm using the average slope of the $c_{t-w}(\lambda)$ spectral dependence presented above. The average value computed within the 0.5–1.5 m near-surface layer is related to the near-surface C_a value (Fig. 10). According to the discrimination line proposed by Loisel and Morel (1998), about 63% of the CoASTS stations revealed a Case-1 behavior (dashed line). Note that this differentiation has been possible for only about half of the data set, that is, when *in situ* measurements of $c_{t-w}(\lambda)$ were available.

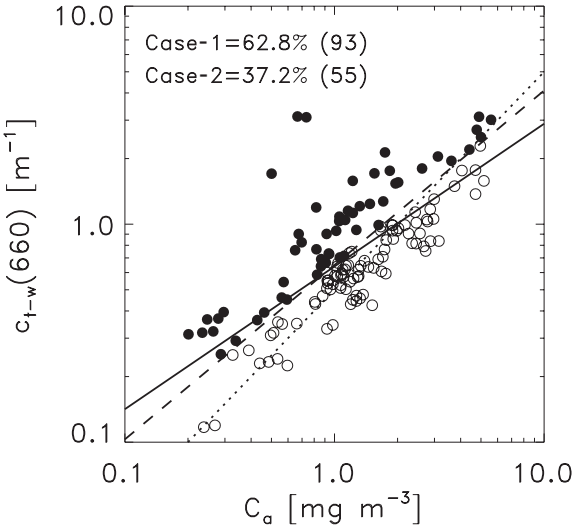

Fig. 10. The relationship, for the near-surface layer, between C_a and the total (except water) beam attenuation coefficient $c_{t-w}(\lambda)$ at 660 nm (average value for a 1 m layer). The solid line represents the linear regression computed for the present data set. The dashed line represents the limit proposed by Loisel and Morel (1998) segregating Case-1 (open circles) and Case-2 (solid circles). The dotted line is the limit adopted by Sagan (1995).

Figure 10 also presents a relationship, $c_{t-w}(660) = 0.5C_a$, of the same type adopted by Mitchell and Holm-Hansen (1991) and Sagan et al. (1995) for classifying Case-1 and Case-2 waters (dotted line) in the Antarctic Peninsula area. Using this latter threshold, the percentage of Case-1 stations for the present study was only 40.5%. The divergence between the two relationships is of particular importance within the C_a interval 0.1–2.0 mg m^{-3}. This illustrates the difficulty in segregating Case-1 and Case-2 waters without ambiguity on the basis of a simple threshold in coastal areas such as the platform site.

4.2 Empirical Algorithms

The potential of this data set for ocean color remote sensing applications in the northern Adriatic Sea was evaluated by examining empirical relationships between surface reflectance and the chlorophyll *a* concentration. Relationships envisaged here involve the in-water remote sensing reflectance, $R_{\rm rs}(\lambda) = L_u(\lambda)/E_d(\lambda)$. As an example, Fig. 11 presents the global relationship for the CoASTS data between C_a (in milligrams per cubic meter) and the reflectance ratio $R_{\rm rs}(490)/R_{\rm rs}(555)$, with the latter denoted in the more compact form $R_{\rm rs}^{3:5}$ for future formulations. As a way of comparison with the SeaWiFS Ocean Color 2 version 4 (OC2v4) algorithm (O'Reilly et al. 2000), a third-order polynomial was fit to the log-transformed (base 10) data and the resulting relationship is:

$$\begin{aligned}\log_{10}[C_a] \;=\; 0.091 \;&-\; 2.620\,\log_{10}\!\left[R_{\rm rs}^{3:5}\right] \\ &-\; 1.148\,\log_{10}\!\left[R_{\rm rs}^{3:5}\right]^2 \\ &-\; 4.949\,\log_{10}\!\left[R_{\rm rs}^{3:5}\right]^3.\end{aligned} \qquad (6)$$

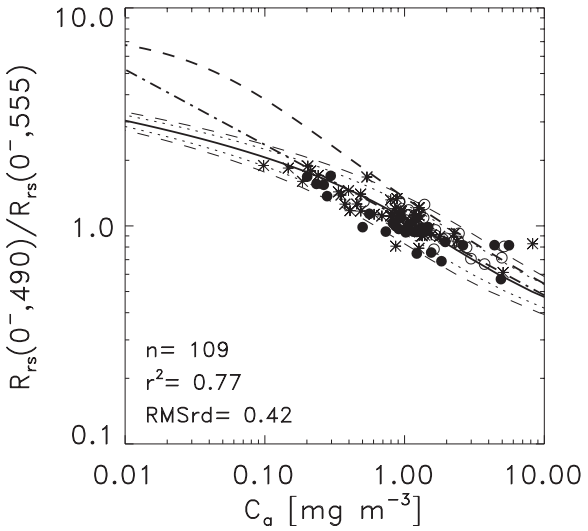

Fig. 11. Relationships between the remote sensing reflectance ratio (0^- depth) $R_{\rm rs}(490)/R_{\rm rs}(555)$ and C_a. Filled and empty circles represent the Case-2 and Case-1 situations, respectively (according to Loisel and Morel 1998), whereas the stars represent the unidentified situations. The thick solid line represents the polynomial fit (see text), the thick dotted-dashed line the linear fit. The dotted and dashed thin lines represent a factor of ±1.5 and ±2 around the fit, respectively. The thick dashed line is the SeaWiFS OC2v4 algorithm.

The global relationship for the CoASTS data set given in (6) explains approximately 77% of the variance in C_a and the root mean square of relative difference (RMSrd) is approximately 42%. In 34 situations out of 109 (i.e., in about 31% of the cases), the fitted C_a values differ from the measured values by more than a factor of 1.5. The OC2v4 algorithm (thick dashed line in Fig. 11) systematically overestimates C_a when applied to the present data set, particularly in the range of 0.1–1.0 mg m^{-3}. For equal C_a values, the corresponding reflectance ratio is lower than that given by the OC2v4 algorithm. The overestimate for the latter is probably because of the increased absorption by dissolved and particulate matter in the blue part of the spectrum. The agreement is much better in the range of 2.0–10.0 mg m^{-3} when C_a is probably the dominating optical component.

For the purposes of comparison with (6), a linear relationship between log-transformed chlorophyll *a* and reflectance values was computed and gives very similar performances (where the determination coefficient r^2 equals 0.76 and RMSrd = 0.43):

$$\log_{10}[C_a] \;=\; 0.079 \;-\; 2.898\,\log_{10}\left[R_{\rm rs}^{3:5}\right]. \qquad (7)$$

The two relationships behave very closely within the range 0.3–10 mg m^{-3} and start to diverge for C_a values lower than 0.3 mg m^{-3} (Fig. 11). The application of these algorithms outside the range used for their development, however, in particular for C_a values lower than 0.1 mg m^{-3}, should be considered with caution.

Note that the use of the subsurface remote sensing reflectance instead of the above-water remote sensing reflectance in such algorithms, does not make an appreciable difference when reflectances are used in ratios. Among the subset of stations for which it was possible (i.e., when AC-9 data were available together with C_a values), the application of the Loisel and Morel (1998) relationship resulted in 49 and 51% of Case-1 (open circles) and Case-2 (solid circles) situations (Fig. 11), respectively.

Figure 12 presents the global relationship between values of $C_{\rm TSM}$ (in grams per cubic meter) and the in-water remote sensing reflectance ratio, $R_{\rm rs}(510)/R_{\rm rs}(665)$, corresponding to the following log-linear fit:

$$\log_{10}[C_{\rm TSM}] \;=\; 0.967 \;-\; 1.169\,\log_{10}\left[\frac{R_{\rm rs}(510)}{R_{\rm rs}(665)}\right]. \qquad (8)$$

This relationship explains 66% of the variance in $C_{\rm TSM}$, with a RMSrd of 39%. In 31 situations out of 109 (about 28%), the fitted $C_{\rm TSM}$ values differ from the measured values by more than a factor of 1.5.

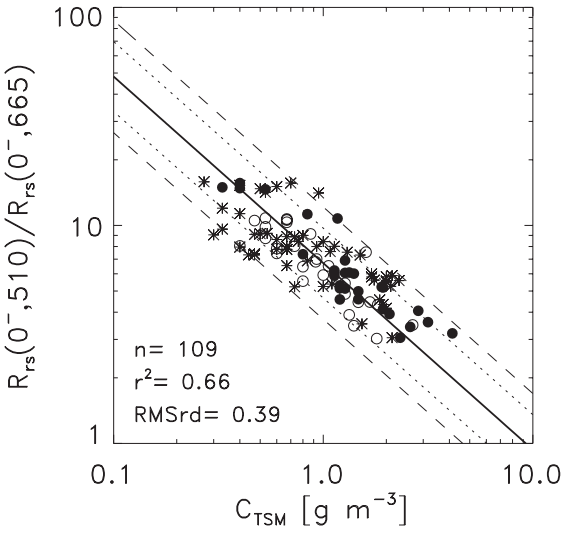

Fig. 12. Relationships between the remote sensing reflectance ratio (0^- depth) $R_{\rm rs}(510)/R_{\rm rs}(665)$ and $C_{\rm TSM}$. The solid line represents the linear fit (see text). The thin dotted and dashed lines and symbols are as in Fig. 11.

The use of other relationships involving more than two reflectances at two different channels was investigated. In particular, multilinear regressions between C_a or $C_{\rm TSM}$ and several reflectances (up to 6) sometimes explained a higher percentage of variance. These relationships, however, have been rejected because of the evidence of high intercorrelation among reflectances, which can lead to a decrease in the predictive power of the relationships. Figure 13 presents the relationship between the ratio of normalized water-leaving radiance $L_{WN}(490)/L_{WN}(555)$ and the diffuse attenuation coefficient for downward irradiance, $K_{E_d}(490)$, computed for an optically homogeneous near-surface layer. The corresponding local algorithm, equivalent to the SeaWiFS algorithm (Mueller 2000) for open ocean application, is the following:

$$K_{E_d}(490) \;=\; 0.016 \;+\; 0.205\left[\frac{L_{WN}(490)}{L_{WN}(555)}\right]^{-1.754}, \qquad (9)$$

where 0.016 m^{-1} is the constant value of $K_{E_d}(490)$ for pure water (adopted by Mueller 2000). This relationship explains 80% of the variance in $K_{E_d}(490)$, with an RMSrd of 23%.

The relatively high scattering of the points in Fig. 13 within the K_{E_d} interval 0.1–0.5 m^{-1} (leading to an r^2 value of only 0.80) may be partly explained by:

- The variability in the relationships between C_a and $C_{\rm TSM}$ (yellow substance influence is relatively lower at these wavelengths), in particular for high concentrations, inducing changes in the radiance spectral shape; and

- The uncertainty in the retrieval of L_{WN} and K_{E_d} in situations of strong vertical (subsurface) stratification.

The slope of the present algorithm is slightly higher than for the SeaWiFS algorithm (−1.5401) proposed by Mueller (2000) and as such, leads to significantly higher values of K_{E_d} for the range 0.2–0.5 m^{-1}. [Actually, the maximum value of $K_{E_d}(490)$ was 0.25 m^{-1} within the data set used to build the SeaWiFS algorithm.]

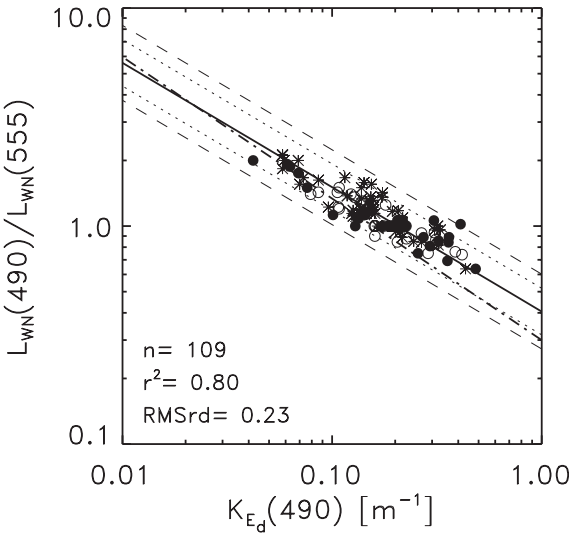

Fig. 13. The relationship between the normalized water-leaving radiance ratio $L_{WN}(490)/L_{WN}(555)$ and the diffuse attenuation coefficient $K_{E_d}(490)$. The solid line represents the fitted power function, the dotted and dashed lines represents a factor of ±1.5 and ±2 around the fit, respectively. The dotted and dashed line represents the Mueller (2000) algorithm. The symbols are as in Fig. 11.

5. CONCLUSIONS

The first three years (from autumn 1995 to autumn 1998) of the CoASTS data collected from an oceanographic tower in the northern Adriatic Sea have been presented and analyzed. The high degree of completeness of the data set, including both marine and atmospheric measurements, makes it appropriate for calibration and validation activities associated with ocean color sensors (Sturm and Zibordi 2002). Care must be taken with the inevitable time lag when creating the matchups between the satellite imagery and the *in situ* measurements, because variability on the scale of one half to one full day cannot be neglected at this site. For the marine components, this short-term variability—mainly affecting the near-surface layer—is superimposed on a classical seasonal variability and is well correlated with salinity variations at the surface resulting from the southward transport of water discharged by rivers into the northern Adriatic Sea.

The concentrations of chlorophyll *a* (C_a) and total suspended matter (C_{TSM}) span over two orders of magnitude. A similar range of expression is observed for the absorption coefficients of particulate and dissolved material. Absorption by pigmented and nonpigmented particulate matter are well correlated with C_a and C_{TSM}, respectively. In addition, the spectral dependence of the absorption coefficients exhibits an appreciable variability (e.g., a factor 2 for the slopes describing the exponential decrease from the blue to the red spectral domain of nonpigmented particulate and of dissolved matter absorption coefficients). Although no measurement of the back-scattering coefficient was undertaken up to the year 2000, the measured particle size distribution could be used within Mie computations to predict the scattering phase function of particles and, hence, the backscattering coefficient. The coefficient of the Junge power law fitted to these size distributions, is in agreement with values previously found for the Mediterranean Sea and also shows a seasonal variability.

The site presents bio-optical characteristics pertaining to both Case-1 (about 63% of the time) and Case-2 (approximately 37% of the time) waters according to the classification relationships between the beam attenuation coefficient at 660 nm, $c_{t-w}(660)$, and the C_a proposed by Loisel and Morel (1998). Nevertheless, it was shown that the classification of coastal areas, such as the platform site, based on a single unique segregation threshold is very challenging. The measured apparent properties [$K_{E_d}(\lambda)$, $Q_n(\lambda)$, $R(\lambda)$, etc.] also encompass a rather wide range of values; their variability is in agreement with the cycle described for the optical components and their inherent optical properties. It has been highlighted that the Q-factor (measured at nadir) shows a significant spectral dependence and that short-term variations, in particular those due to changes in the water content, are superimposed over the seasonal cycle (mostly defined by the average sun zenith cycle).

The local empirical algorithm making use of the ratio $R_{\mathrm{rs}}(490)/R_{\mathrm{rs}}(555)$ explains 77% of the variance in the C_a near-surface concentration and is likely to provide lower values (by a factor of 2–4) in the range of 0.1–1.0 mg m^{-3} than the SeaWiFS OC2v4 algorithm, whereas the two algorithms converge in the range 1.0–10.0 mg m^{-3}. A local empirical algorithm making use of the ratio $R_{\mathrm{rs}}(510)/R_{\mathrm{rs}}(665)$ explains 66% of the variance in the C_{TSM} near-surface concentration. The algorithm using the ratio of normalized water-leaving radiances $L_{WN}(490)/L_{WN}(555)$ explains 80% of the variance in $K_{E_d}(490)$. The rather large range of C_a values covered by the data set probably makes the C_a algorithm applicable to the whole northern Adriatic Sea with the possible exception of some unique situations, such as, the area very close to the coast or in near proximity to river plumes (e.g., the Po River plume).

Acknowledgments

The constitution of this data set would not have been possiblewithout the contribution of the following people: Luigi Alberotanza, Pier Luigi Cova, Massimo Ferrari, Claudia Ramasco,

Barbara Sapino, and Allessandro Vianello. Their work is duly acknowledged. Particular acknowledgment is also due to the tower crew, Armando Penzo, Narciso Zennaro, Daniele Penzo, and Gianni Zennaro for their significant logistic support during each field campaign. Many thanks also to Davide D'Alimonte who ultimately contributed to data processing and to Stanford Hooker for early comments on the manuscript. Warm acknowledgements are finally due to Peter Schlittenhardt for the continuous support he has always given to the CoASTS personnel and activities.

This work is partially supported by the European Commission under contracts ENV4CT960307 and MAS3CT970087, and by NASA through grant NCC5-371.

Glossary

AAOT	*Acqua Alta* Oceanographic Tower
AERONET	Aerosol Robotic Network
AMJ	April–May–June
AMT	Atlantic Meridional Transect
CoASTS	Coastal Atmosphere and Sea Time Series
CTD	Conductivity, Temperature, and Depth
CZCS	Coastal Zone Color Scanner
GSFC	Goddard Space Flight Center
HPLC	High Performance Liquid Chromatography
IOCCG	International Ocean Colour Coordinating Group
JGOFS	Joint Global Ocean Flux Study
JAS	July–August–September
JFM	January–February–March
MERIS	Medium Resolution Imaging Spectrometer
MOBY	Marine Optical Buoy
MODIS	Moderate Resolution Imaging Spectroradiometer
MOS	Modular Opto-electronic Sensor
NAd	North Adriatic (Current)
NASA	National Aeronautics and Space Administration
OC2v4	Ocean Chlorophyll 2 (algorithm) version 4
OCI	Ocean Color Irradiance
OCR	Ocean Color Radiance
OCTS	Ocean Color and Temperature Scanner
OND	October–November–December
PlyMBODy	Plymouth Marine Bio-Optical Data Buoy
PSU	Practical Salinity Units
RMSrd	Root Mean Square of relative difference
SeaWiFS	Sea-viewing Wide Field-of-view Sensor
TSM	Total Suspended Matter
UNESCO	United Nations Educational, Scientific, and Cultural Organization
YBOM	Yamato Bank Optical Mooring

Symbols

$a_{dp}(\lambda)$	Nonpigmented particulate matter absorption coefficient.
$a_p(\lambda)$	Total particulate matter absorption coefficient.
$a_{ph}(\lambda)$	Pigmented particulate matter absorption coefficient.
$a^*_{ph}(\lambda)$	Chorophyll *a*-specific pigmented particulate matter absorption coefficient.
$a_{t-w}(\lambda)$	Total (except water) absorption coefficient.
$a_{ys}(\lambda)$	Colored dissolved organic matter (yellow substance) absorption coefficient.
a_{yxx}	Generic symbol for a_{0dp} or a_{0ys}.
a_{0dp}	Coefficient of $a_{dp}(\lambda)$ exponential law.
a_{0ys}	Coefficient of $a_{ys}(\lambda)$ exponential law.
$b(\lambda)$	Total scattering coefficient.
$b_{t-w}(\lambda)$	Total (except water) scattering coefficient.
$c(\lambda)$	Total beam attenuation coefficient.
$c_{t-w}(\lambda)$	Total (except water) beam attenuation coefficient.
cb_{dp}	Background of $a_{dp}(\lambda)$ exponential law.
cb_{ys}	Background of $a_{ys}(\lambda)$ exponential law.
cb_{xx}	Either cb_{dp} or cb_{ys}.
C	Pigment concentration.
C_a	Chlorophyll *a* concentration.
C_A	Alloxanthin concentration.
C_b	Chlorophyll *b* concentration.
C_d	Diatoxanthin concentration.
C_D	Diadinoxanthin concentration.
C_F	Fucoxanthin concentration.
C_{HB}	The sum of the 19′-hexanoyloxyfucoxanthin and 19′-butanoyloxyfucoxanthin concentrations.
C_{TSM}	Total suspended matter concentration.
C_Z	Zeaxanthin concentration.
C_{12}	Chlorophyll $c_1 + c_2$ concentration.
D	Particle diameter.
$E_d(z,\lambda)$	Downward irradiance at depth z.
$E_d(0^-,\lambda)$	Subsurface downward irradiance.
$E_u(z,\lambda)$	Upward irradiance at depth z.
$E_u(0^-,\lambda)$	Subsurface upward irradiance.
k	Junge coefficient.
$K_{E_d}(\lambda)$	Diffuse attenuation coefficient of $E_d(z,\lambda)$.
$L_u(z,\lambda)$	Upwelling radiance at depth z.
$L_u(0^-,\lambda)$	Subsurface upwelling radiance.
$L_{WN}(\lambda)$	Normalized water leaving radiance.
m	Air mass.
n	Number of samples.
N	Number of particles of diameter D.
N_0	Concentration of particles.
nb	Exponent of the $b_{t-w}(\lambda)$ power function.
P_a	Atmospheric pressure.
$Q_n(0^-,\lambda)$	Q-factor for nadir, $Eu(0^-,\lambda)/Lu(0^-,\lambda)$.
r^2	Determination coefficient.
$R(0^-,\lambda)$	In-water reflectance, $E_u(0^-,\lambda)/E_d(0^-,\lambda)$.
$R_{\mathrm{rs}}(0^-,\lambda)$	In-water remote sensing reflectance, defined as the $L_u(0^-,\lambda)/E_d(0^-,\lambda)$ ratio.
$R^{3:5}_{\mathrm{rs}}$	The $R_{\mathrm{rs}}(0^-,490)/R_{\mathrm{rs}}(0^-,555)$ ratio.
RH	Relative humidity.
S_{dp}	Slope of $a_{dp}(\lambda)$ exponential law.
S_w	Seawater salinity.
S_{xx}	Either S_{dp} or S_{ys}.
S_{ys}	Slope of $a_{ys}(\lambda)$ exponential law.
T_a	Air temperature.
T_w	Water temperature.
W_d	Wind direction.
W_s	Wind speed.
xx	Generic symbol for dp or ys.
$\bar{X}$	The average value of variable X.
X^-	The minimum value of variable X.
X^+	The maximum value of variable X.
X_n	The number of samples for variable X.
X_σ	The standard deviation of variable X.

z Depth.
α Ångström exponent.
β Ångström coefficient.
γ Density excess.
λ Wavelength.
λ_0 Reference wavelength.
ξ Junge exponent.
σ Standard deviation.
$\tau_a(\lambda)$ Aerosol optical thickness.
χ^2 Chi squared.

References

Aiken, J., N. Rees, S. Hooker, P. Holligan, A. Bale, D. Robins, G. Moore, R. Harris, and D. Pilgrim, 2000: The Atlantic Meridional Transect: Overview and synthesis of data. *Prog. Oceanogr.,* (Special Issue on the Atlantic Meridional Transect), **45,** 257–312.

Ångström, A., 1961: Techniques of determining the turbidity of the atmosphere. *Tellus,* **13,** 214–223.

Artegiani, A., D. Bregant, E. Paschini, N. Pinardi, F. Raicich, and A. Russo, 1997a: The Adriatic Sea general circulation, Part I: Air–sea interactions and water mass structure. *J. Phys. Oceanogr.,* **27,** 1,492–1,514.

——, ——, ——, ——, ——, and ——, 1997b: The Adriatic Sea general circulation, Part II: Baroclinic circulation structure. *J. Phys. Oceanogr.,* **27,** 1,515–1,532.

Berthon, J-F., M. Babin, A. Morel, and H. Claustre, 1995: Variability in the chlorophyll-specific absorption coefficients of natural phytoplankton: Analysis and parameterization. *J. Geophys. Res.,* **100,** 13,321–13,332.

——, G. Zibordi, S. Grossi, D. van der Linde, and C. Targa, 1998: The CoASTS time-series of bio-optical measurements in the North Adriatic Sea: An analysis in view to interpretation of satellite color data in coastal waters. *Ocean Optics XIV,* Kailua-Kona, USA, 10–13 November 1998.

——, ——, and S. Hooker, 2000: Optical measurements during a "mucilage" event in the North Adriatic Sea. *Limnol. Oceanogr.,* **45,** 322–327.

——, ——, D. D'Alimonte, S. Grossi, D. van der Linde, and C. Targa, 2001: Empirical relationships between apparent and inherent optical properties in the northern Adriatic Sea. Proc. Int. Conf. Current Problems in Optics of Natural Waters (ONW'2001), 25–28 September 2001, St. Petersburg, Russia, *Proc. D.S. Rozhdestvensky Opt. Soc.,* 311–317.

Bricaud, A., M. Babin, A. Morel, and H. Claustre, 1995: Variability in the chlorophyll-specific absorption coefficients of natural phytoplankton: Analysis and parameterization. *J. Geophys. Res.,* **100,** 13,321–13,332.

Bustillos-Guzmán, J., H. Claustre, and J.C. Marty, 1995: Specific phytoplankton signatures and their relationship to hydrographic conditions in the coastal northwestern Mediterranean Sea. *Mar. Ecol. Prog. Ser.,* **124,** 247–258.

Carder, K.L., S.K. Hawes, K.A. Baker, R.C. Smith, R.G. Steward, and B.G. Mitchell, 1991: Reflectance model for quantifying chlorophyll *a* in the presence of productivity degradation products. *J. Geophys. Res.,* **96,** 20,599–20,611.

——, F.R. Chen, Z.P. Lee, and S.K. Hawes, 1999: Semi-analytic Moderate-Resolution Imaging Spectrometer algorithms for chlorophyll *a* and absorption with bio-optical domains based on nitrate-depletion temperatures. *J. Geophys. Res.,* **104,** 5,403–5,421.

Clark, D.K., H.R. Gordon, K.J. Voss, Y. Ge, W. Broenkow, and C. Trees, 1997: Validation of atmospheric correction over the oceans. *J. Geophys. Res.,* **102,** 17,209–17,217.

Claustre, H., P. Kerhervé, J-C. Marty, L. Prieur, and J.H. Hecq, 1994: Phytoplankton distribution associated with a geostrophic front: ecological and biogeochemical implications. *J. Mar. Res.,* **52,** 711–742.

De Santis, L.V., C. Tomasi, and V. Vital, 1994: Characterization of Ångström's turbidity parameters in the Po Valley area for summer conditions of the atmosphere. *Il Nuovo Cimento,* **17C,** 407–430.

Diehl, H.P., and H. Haardt, 1980: Measurement of the spectral attenuation to support biological research in a "plankton tube" experiment. *Oceanol. Acta,* **3,** 89–96.

Doyle, J.P., and G. Zibordi, 2002: Monte Carlo modelling of optical transmission within 3-D shadowed field: application to large deployment structures. *Appl. Opt.,* (in press).

Ferrari, G.M., M.D. Dowell, S. Grossi, and C. Targa, 1996: Relationship between the optical properties of chromophoric dissolved organic matter and total concentration of dissolved organic carbon in the southern Baltic Sea region. *Mar. Chem.,* **55,** 299–316.

Gilmartin, M., and N. Revelante, 1980: Nutrient input and the summer nanoplankton bloom in the northern Adriatic Sea. *Mar. Ecol.,* **1,** 169–180.

——, D. Degobbis, N. Relevante, and N. Smodlaka, 1990: The mechanism controlling plant nutrient concentrations in the Northern Adriatic Sea. *Int. Revue Ges. Hydrobiol.,* **75,** 425–445.

Green, S.A., and N. Blough, 1994: Optical absorption and fluorescence properties of chromophoric dissolved organic matter in natural waters. *Limnol. Oceanogr.,* **39,** 1,903–1,916.

Gould, R.W., R.A. Arnone, and P.M. Martinolich, 1999: Spectral dependence of the scattering coefficient in Case-1 and Case-2 waters. *Appl. Opt.,* **38,** 2,377–2,383.

Holben, B.N., T.F. Eck, I. Slutsker, D. Tanré, J-P. Buis, A. Setzer, E. Vermote, J.A. Reagan, Y.J. Kaufman, T. Nakajima, F. Lavenu, I. Jankowiak, and A. Smirnov, 1998: AERONET—A federated instrument network and data archive for aerosol characterization. *Remote Sens. Environ.,* **66,** 1–16.

Hooker, S.B., W.E. Esaias, G.C. Feldman, W.W. Gregg, and C.R. McClain, 1992: An Overview of SeaWiFS and Ocean Color. *NASA Tech. Memo. 104566, Vol. 1,* S.B. Hooker and E.R. Firestone, Eds., NASA Goddard Space Flight Center, Greenbelt, Maryland, 24 pp.

IOCCG, 1998: Minimum Requirements for an Operational Ocean Colour Sensor for the open ocean. *Reports Int. Ocean-Colour Coordinating Group, Report Number 1,* 46 pp.

JGOFS, 1994: Protocols for the Joint Global Ocean Flux Study Core Measurements. Intergovernmental Oceanographic Commission, *Scientific Committee on Oceanic Research, Manual and Guides,* UNESCO, **29,** 91–96.

Jonasz, M., 1983: Particle-size distributions in the Baltic. *Tellus,* **35B,** 346–358.

Junge, C.E., 1963: Air chemistry and radioactivity. Academic Press, New York, 382 pp.

Kahru, M., and B.G. Mitchell, 1999: Empirical chlorophyll algorithm and preliminary SeaWiFS validation for the California Current. *Int. J. Remote Sens.,* **20,** 3,423–3,429.

Kirk, J.T.O., 1994: *Light and Photosynthesis in Aquatic Ecosystems.* 2nd ed., Cambridge University Press, Cambridge, United Kingdom, 509 pp.

Kishino, M., J. Ishizaka, S. Saitoh, Y. Senga, and M. Utashima, 1997: Verification plan of Ocean Color and Temperature Scanner atmospheric correction and phytoplankton pigment by moored optical buoy system. *J. Geophys. Res.,* **102,** 17,197–17,207.

Loisel, H., and A. Morel, 1998: Light scattering and chlorophyll concentration in Case-1 waters: A reexamination. *Limnol. Oceanogr.,* **43,** 847–858.

Maritorena, S., A. Morel, and B. Gentili, 1994: Diffuse reflectance of oceanic shallow water: influence of water depth and bottom albedo. *Limnol. Oceanogr.,* **39,** 1,689–1,703.

Mitchell, B.G., and D.A. Kiefer, 1988: Variability in the pigment specific fluorescence and absorption spectra in the northeastern Pacific Ocean. *Deep-Sea Res.,* Part A, **35,** 665–689.

——, and O. Holm-Hansen, 1991: Bio-optical properties of Antarctic Peninsula waters: differentiation from temperate ocean models. *Deep-Sea Res.,* **38,** 1,009–1,028.

Morel, A., and L. Prieur, 1977: Analysis of variations in ocean color. *Limnol. Oceanogr.,* **22,** 709–722.

——, and A. Bricaud, 1981: Theoretical results concerning light absorption in a discrete medium, and application to specific absorption by phytoplankton. *Deep-Sea Res.,* **28,** 1,375–1,393.

——, and B. Gentili, 1996: Diffuse reflectance of oceanic waters. III. Implication of bidirectionality for the remote-sensing problem. *Appl. Opt.,* **35,** 4,850–4,862.

Mueller, J.L., 2000: "SeaWiFS algorithm for the diffuse attenuation coefficient, $K(490)$, using water-leaving radiances at 490 and 555 nm." In: O'Reilly, J.E., and 24 Coauthors, SeaWiFS Postlaunch Calibration and Validation Analyses, Part 3, *NASA Tech. Memo. 2000–206892, Vol. 11,* S.B. Hooker and E.R. Firestone, Eds., NASA Goddard Space Flight Center, Greenbelt, Maryland, 24–27.

O'Reilly, J.E., S. Maritorena, B.G. Mitchell, D.A. Siegel, K.L. Carder, S.A. Garver, M. Kahru, and C. McClain, 1998: Ocean Color chlorophyll algorithms for SeaWiFS. *J. Geophys. Res.,* **103,** 24,937–24,953.

——, and 21 Coauthors, 2000: "Ocean color chlorophyll a algorithm for SeaWiFS, OC2 and OC4: Version 4." In: O'Reilly, J.E., and 21 Coauthors, SeaWiFS Postlaunch Calibration and Validation Analyses, Part 3, *NASA Tech. Memo. 2000–206892, Vol. 11,* S.B. Hooker and E.R. Firestone, Eds., NASA Goddard Space Flight Center, Greenbelt, Maryland, 9–23.

Pinkerton, M., and J. Aiken, 1999: Calibration and validation of remotely-sensed observations of ocean colour from a moored data buoy. *J. Atmos. Oceanic. Tech.,* **16,** 915–923.

Reuter, R., 1980: Characterization of marine particle suspensions by light scattering. II. Experimental results. *Oceanol. Acta,* **3,** 325–332.

Sagan, S., A.R. Weeks, I.S. Robinson, G.F. Moore, and J. Aiken, 1995: The relationships between the beam attenuation coefficient and chlorophyll concentration and reflectance in Antarctic waters. *Deep-Sea Res.,* **42,** 983–996.

Smith, R.C., and K.S. Baker, 1978: Optical classification of natural waters. *Limnol. Oceanogr.,* **23,** 260–267.

Stramski, D., and D.A. Kiefer, 1991: Light scattering by microorganisms in the open ocean. *Prog. Oceanogr.,* **28,** 343–383.

Strickland, J.D.H., and T.R. Parsons, 1972: A practical handbook of sea water analysis. 2nd ed., *Fish. Res. Board Canada,* **167,** 181–184.

Sturm, B., and G. Zibordi, 2002: SeaWiFS atmospheric corrections by an approximate model and vicarious calibration, *Int. J. Remote. Sens.,* **23,** 489–501.

Tassan, S., and G.M. Ferrari, 1995: An alternative approach to absorption measurements of aquatic particles retained on filters. *Limnol. Oceanogr.,* **40,** 1,358–1,368.

UNESCO, 1981: Tenth report of the joint panel on oceanographic tables and standards. Sidney, British Columbia, September 1980, *UNESCO Tech. Papers Mar. Sci.,* **36,** 25 pp.

Voss, K.J., 1992: A spectral model of the beam attenuation coefficient in the ocean and coastal areas, *Limnol. Oceanogr.,* **37,** 501–509.

Zaneveld, J.R.V., J.C. Kitchen, A. Bricaud, and C. Moore, 1992: Analysis of *in situ* spectral absorption meter data. Ocean Optics XI, *Proc. SPIE,* **1750,** 187–200.

Zavatarelli, M., F. Raicich, D. Bregant, A. Russo, and A. Artegiani, 1998: Climatological biogeochemical characteristics of the Adriatic Sea. *J. Mar. System,* **18,** 227–263.

Zibordi, G., and M. Ferrari, 1995: Instrument self-shading in underwater optical measurements: experimental data. *Appl. Opt.,* **34,** 2,750–2,754.

——, J-P. Doyle, and S.B. Hooker, 1999: Offshore tower shading effects on in-water optical measurements. *J. Atmos. Ocean. Tech.,* **16,** 1,767–1,779.

——, and J-F. Berthon, 2001: Relationships between the Q-factor and seawater optical properties in a coastal region. *Limnol. Oceanogr.,* **46,** 1,130–1,140.

——, ——, J-P. Doyle, S. Grossi, D. van der Linde, C. Targa, and L. Alberotanza, 2002: Coastal Atmosphere and Sea Time-series (CoASTS), Part 1: A Tower-Based Long-Term Measurement Program. *NASA Tech. Memo. 2002–206892, Vol. 19,* S.B. Hooker and E.R. Firestone, Eds., NASA Goddard Space Flight Center, Greenbelt, Maryland, 29 pp.

The SeaWiFS Postlaunch Technical Report Series

Vol. 1

Johnson, B.C., J.B. Fowler, and C.L. Cromer, 1998: The SeaWiFS Transfer Radiometer (SXR). *NASA Tech. Memo. 1998–206892, Vol. 1,* S.B. Hooker and E.R. Firestone, Eds., NASA Goddard Space Flight Center, Greenbelt, Maryland, 58 pp.

Vol. 2

Aiken, J., D.G. Cummings, S.W. Gibb, N.W. Rees, R. Woodd-Walker, E.M.S. Woodward, J. Woolfenden, S.B. Hooker, J-F. Berthon, C.D. Dempsey, D.J. Suggett, P. Wood, C. Donlon, N. González-Benítez, I. Huskin, M. Quevedo, R. Barciela-Fernandez, C. de Vargas, and C. McKee, 1998: AMT-5 Cruise Report. *NASA Tech. Memo. 1998–206892, Vol. 2,* S.B. Hooker and E.R. Firestone, Eds., NASA Goddard Space Flight Center, Greenbelt, Maryland, 113 pp.

Vol. 3

Hooker, S.B., G. Zibordi, G. Lazin, and S. McLean, 1999: The SeaBOARR-98 Field Campaign. *NASA Tech. Memo. 1999–206892, Vol. 3,* S.B. Hooker and E.R. Firestone, Eds., NASA Goddard Space Flight Center, Greenbelt, Maryland, 40 pp.

Vol. 4

Johnson, B.C., E.A. Early, R.E. Eplee, Jr., R.A. Barnes, and R.T. Caffrey, 1999: The 1997 Prelaunch Radiometric Calibration of SeaWiFS. *NASA Tech. Memo. 1999–206892, Vol. 4,* S.B. Hooker and E.R. Firestone, Eds., NASA Goddard Space Flight Center, Greenbelt, Maryland, 51 pp.

Vol. 5

Barnes, R.A., R.E. Eplee, Jr., S.F. Biggar, K.J. Thome, E.F. Zalewski, P.N. Slater, and A.W. Holmes 1999: The SeaWiFS Solar Radiation-Based Calibration and the Transfer-to-Orbit Experiment. *NASA Tech. Memo. 1999–206892, Vol. 5,* S.B. Hooker and E.R. Firestone, Eds., NASA Goddard Space Flight Center, 28 pp.

Vol. 6

Firestone, E.R., and S.B. Hooker, 2000: SeaWiFS Postlaunch Technical Report Series Cumulative Index: Volumes 1–5. *NASA Tech. Memo. 2000–206892, Vol. 6,* S.B. Hooker and E.R. Firestone, Eds., NASA Goddard Space Flight Center, Greenbelt, Maryland, 14 pp.

Vol. 7

Johnson, B.C., H.W. Yoon, S.S. Bruce, P-S. Shaw, A. Thompson, S.B. Hooker, R.E. Eplee, Jr., R.A. Barnes, S. Maritorena, and J.L. Mueller, 1999: The Fifth SeaWiFS Intercalibration Round-Robin Experiment (SIRREX-5), July 1996. *NASA Tech. Memo. 1999–206892, Vol. 7,* S.B. Hooker and E.R. Firestone, Eds., NASA Goddard Space Flight Center, 75 pp.

Vol. 8

Hooker, S.B., and G. Lazin, 2000: The SeaBOARR-99 Field Campaign. *NASA Tech. Memo. 2000–206892, Vol. 8,* S.B. Hooker and E.R. Firestone, Eds., NASA Goddard Space Flight Center, 46 pp.

Vol. 9

McClain, C.R., E.J. Ainsworth, R.A. Barnes, R.E. Eplee, Jr., F.S. Patt, W.D. Robinson, M. Wang, and S.W. Bailey, 2000: SeaWiFS Postlaunch Calibration and Validation Analyses, Part 1. *NASA Tech. Memo. 2000–206892, Vol. 9,* S.B. Hooker and E.R. Firestone, Eds., NASA Goddard Space Flight Center, 82 pp.

Vol. 10

McClain, C.R., R.A. Barnes, R.E. Eplee, Jr., B.A. Franz, N.C. Hsu, F.S. Patt, C.M. Pietras, W.D. Robinson, B.D. Schieber, G.M. Schmidt, M. Wang, S.W. Bailey, and P.J. Werdell, 2000: SeaWiFS Postlaunch Calibration and Validation Analyses, Part 2. *NASA Tech. Memo. 2000–206892, Vol. 10,* S.B. Hooker and E.R. Firestone, Eds., NASA Goddard Space Flight Center, 57 pp.

Vol. 11

O'Reilly, J.E., S. Maritorena, M.C. O'Brien, D.A. Siegel, D. Toole, D. Menzies, R.C. Smith, J.L. Mueller, B.G. Mitchell, M. Kahru, F.P. Chavez, P. Strutton, G.F. Cota, S.B. Hooker, C.R. McClain, K.L. Carder, F. Müller-Karger, L. Harding, A. Magnuson, D. Phinney, G.F. Moore, J. Aiken, K.R. Arrigo, R. Letelier, and M. Culver 2000: SeaWiFS Postlaunch Calibration and Validation Analyses, Part 3. *NASA Tech. Memo. 2000–206892, Vol. 11,* S.B. Hooker and E.R. Firestone, Eds., NASA Goddard Space Flight Center, 49 pp.

Vol. 12

Firestone, E.R., and S.B. Hooker, 2000: SeaWiFS Postlaunch Technical Report Series Cumulative Index: Volumes 1–11. *NASA Tech. Memo. 2000–206892, Vol. 12,* S.B. Hooker and E.R. Firestone, Eds., NASA Goddard Space Flight Center, Greenbelt, Maryland, 24 pp.

Vol. 13

Hooker, S.B., G. Zibordi, J-F. Berthon, S.W. Bailey, and C.M. Pietras, 2000: The SeaWiFS Photometer Revision for Incident Surface Measurement (SeaPRISM) Field Commissioning. *NASA Tech. Memo. 2000–206892, Vol. 13,* S.B. Hooker and E.R. Firestone, Eds., NASA Goddard Space Flight Center, Greenbelt, Maryland, 24 pp.

Vol. 14

Hooker, S.B., H. Claustre, J. Ras, L. Van Heukelem, J-F. Berthon, C. Targa, D. van der Linde, R. Barlow, and H. Sessions, 2000: The First SeaWiFS HPLC Analysis Round-Robin Experiment (SeaHARRE-1). *NASA Tech. Memo. 2000–206892, Vol. 14,* S.B. Hooker and E.R. Firestone, Eds., NASA Goddard Space Flight Center, Greenbelt, Maryland, 42 pp.

Vol. 15

Hooker, S.B., G. Zibordi, J-F. Berthon, D. D'Alimonte, S. Maritorena, S. McLean, and J. Sildam, 2001: Results of the Second SeaWiFS Data Analysis Round Robin, March 2000 (DARR-00). *NASA Tech. Memo. 2001–206892, Vol. 15,* S.B. Hooker and E.R. Firestone, Eds., NASA Goddard Space Flight Center, Greenbelt, Maryland, 71 pp.

Vol. 16

Patt, F.S., 2002: Navigation Algorithms for the SeaWiFS Mission. *NASA Tech. Memo. 2002–206892, Vol. 16,* S.B. Hooker and E.R. Firestone, Eds., NASA Goddard Space Flight Center, Greenbelt, Maryland, 17 pp.

Vol. 17

Hooker, S.B., S. McLean, J. Sherman, M. Small, G. Lazin, G. Zibordi, and J.W. Brown, 2002: The Seventh SeaWiFS Intercalibration Round-Robin Experiment (SIRREX-7), March 1999. *NASA Tech. Memo. 2002–206892, Vol. 17,* S.B. Hooker and E.R. Firestone, Eds., NASA Goddard Space Flight Center, Greenbelt, Maryland, 69 pp.

Vol. 18

Firestone, E.R., and S.B. Hooker, 2002: SeaWiFS Postlaunch Technical Report Series Cumulative Index: Volumes 1–17. *NASA Tech. Memo. 2002–206892, Vol. 18,* S.B. Hooker and E.R. Firestone, Eds., NASA Goddard Space Flight Center, Greenbelt, Maryland, (in preparation).

Vol. 19

Zibordi, G., J-F. Berthon, J.P. Doyle, S. Grossi, D. van der Linde, C. Targa, and L. Alberotanza 2002: Coastal Atmosphere and Sea Time Series (CoASTS), Part 1: A Tower-Based Long-Term Measurement Program. *NASA Tech. Memo. 2002–206892, Vol. 19,* S.B. Hooker and E.R. Firestone, Eds., NASA Goddard Space Flight Center, Greenbelt, Maryland, 29 pp.

Vol. 20

Berthon, J-F., G. Zibordi, J.P. Doyle, S. Grossi, D. van der Linde, and C. Targa, 2002: Coastal Atmosphere and Sea Time Series (CoASTS), Part 2: Data Analysis. *NASA Tech. Memo. 2002–206892, Vol. 20,* S.B. Hooker and E.R. Firestone, Eds., NASA Goddard Space Flight Center, Greenbelt, Maryland, 25 pp.